Review

Probing Biomolecular Interactions at Conductive and Semiconductive Surfaces by Impedance Spectroscopy: Routes to Impedimetric Immunosensors, DNA-Sensors, and Enzyme Biosensors

*Eugenii Katz**, *Itamar Willner*

Institute of Chemistry, The Hebrew University of Jerusalem, Jerusalem 91904, Israel
* e-mail: ekatz@vms.huji.ac.il; willnea@vms.huji.ac.il

Received: December 18, 2002
Final version: February 3, 2003

Abstract
Impedance spectroscopy is a rapidly developing electrochemical technique for the characterization of biomaterial-functionalized electrodes and biocatalytic transformations at electrode surfaces, and specifically for the transduction of biosensing events at electrodes or field-effect transistor devices. The immobilization of biomaterials, e.g., enzymes, antigens/antibodies or DNA on electrodes or semiconductor surfaces alters the capacitance and interfacial electron transfer resistance of the conductive or semiconductive electrodes. Impedance spectroscopy allows analysis of interfacial changes originating from biorecognition events at electrode surfaces. Kinetics and mechanisms of electron transfer processes corresponding to biocatalytic reactions occurring at modified electrodes can be also derived from Faradaic impedance spectroscopy. Different immunosensors that use impedance measurements for the transduction of antigen-antibody complex formation on electronic transducers were developed. Similarly, DNA biosensors using impedance measurements as readout signals were developed. Amplified detection of the analyte DNA using Faradaic impedance spectroscopy was accomplished by the coupling of functionalized liposomes or by the association of biocatalytic conjugates to the sensing interface providing biocatalyzed precipitation of an insoluble product on the electrodes. The amplified detections of viral DNA and single-base mismatches in DNA were accomplished by similar methods. The changes of interfacial features of gate surfaces of field-effect transistors (FET) upon the formation of antigen-antibody complexes or assembly of protein arrays were probed by impedance measurements and specifically by transconductance measurements. Impedance spectroscopy was also applied to characterize enzyme-based biosensors. The reconstitution of apo-enzymes on cofactor-functionalized electrodes and the formation of cofactor-enzyme affinity complexes on electrodes were probed by Faradaic impedance spectroscopy. Also biocatalyzed reactions occurring on electrode surfaces were analyzed by impedance spectroscopy. The theoretical background of the different methods and their practical applications in analytical procedures were outlined in this article.

Keywords: Impedance spectroscopy, Biosensor, Immunosensor, DNA sensor, Enzyme, Field-effect transistor, Capacitance, Bioelectronics

1. Introduction

Bioelectronics is a rapidly progressing field at the junction of chemistry, biochemistry, physics, and material science [1]. The basic feature of a bioelectronic device is the interaction of a biomaterial with a conductive or semiconductive support, and the electronic transduction of the biological functions associated with the biological matrices. Biomaterials that can be interacted with electronic transducers include proteins, that is, enzymes [2–4], receptors [5, 6], antibodies or antigens [7–10], oligonucleotides or DNA fragments [11–13], or low molecular weight molecules exhibiting affinity interactions with other biomaterials such as cofactors, namely, $NAD(P)^+$ [14], biotin [15], or, for example, saccharides exhibiting affinity interactions with lectins [16]. Different electronic methods were employed to transduce the biological functions occurring at the electronic supports [17]. These include electrical transduction, such as current [18], potential changes [19, 20], piezoelectric transduction [21–24], field-effect transistor (FET) transduction [25, 26], photoelectrochemical transduction [27] and others [28–33]. Many of the biosensor devices involve the formation of a recognition complex between the sensing biomaterial and the analyte in a monolayer or thin film configuration on the electronic transducer [34]. Formation of the complex on a conductive or semiconductive surface alters the capacitance and the resistance at the surface-electrolyte interface. Furthermore, the build-up of the sensing biomaterial film on the conductive or semiconductive support alters the capacitance and resistance properties of the solid support-electrolyte interface. Impedance spectroscopy is a very powerful tool for the analysis of interfacial properties changes of modified electrodes upon biorecognition events occurring at the modified surfaces. Impedance

  1040-0397/03/1106-0913 $ 17.50+.50/0

measurements provide detailed information on capacitance/resistance changes occurring at conductive or semiconductive surfaces. Thus, impedance spectroscopy [35, 36], including non-Faradaic impedance measurements resulting in capacitance sensing [37], is becoming an attractive electrochemical tool to characterize biomaterial films associated with electronic elements, thus, allowing transduction of biorecognition events at the respective surfaces. Faradaic impedance spectroscopy allows analysis of kinetics and mechanisms of bioelectrocatalytic reactions at the modified electrode surfaces providing important information for the development of amperometric biosensors and biofuel cells.

The present article addresses recent advances in the application of the impedance spectroscopy to various kinds of biosensors, including immunosensors, DNA-sensors, and enzyme-based sensors, as well as outlines different kinds of the impedance spectroscopy, such as non-Faradaic capacitance measurements, Faradaic impedance spectroscopy in the presence of an external redox label, in-plane alternative voltage conductivity measurements, and transconductance measurements with field-effect transistors. The article includes a theoretical background important to understand the analytical applications of impedance measurements and an overview of the experimental results exemplifying specific biosensor systems.

2. Impedance Spectroscopy – Theoretical Background

Impedance spectroscopy is an effective method for probing the features of surface-modified electrodes [38, 39]. A small-amplitude perturbing sinusoidal voltage signal is applied to the electrochemical cell, and the resulting current response is measured. The impedance is calculated as the ratio between the system voltage phasor, $U(j\omega)$, and the current phasor, $I(j\omega)$, which are generated by a frequency response analyzer during the experiment, Equation 1, where $j = \sqrt{-1}$ and ω and f (excitation frequency) have units of $rad \cdot s^{-1}$ and Hz, respectively. The complex impedance can be presented as the sum of the real, $Z_{re}(\omega)$, and imaginary, $Z_{im}(\omega)$ components that originate mainly from the resistance and capacitance of the cell, respectively.

$$Z(j\omega) = \frac{U(j\omega)}{I(j\omega)} = Z_{re}(\omega) + jZ_{im}(\omega); \quad \text{where } \omega = 2\pi f \quad (1)$$

Electrochemical transformations occurring at the electrode/electrolyte interface can be modeled by extracting components of the electronic equivalent circuits that correspond to the experimental impedance spectra. A general electronic equivalent circuit (Randles and Ershler model [38–41]), which is very often used to model interfacial phenomena, includes the ohmic resistance of the electrolyte solution, R_s, the Warburg impedance, Z_W, resulting from the diffusion of ions from the bulk electrolyte to the electrode interface, the double layer capacitance, C_{dl}, and electron transfer resistance, R_{et}, that exists if a redox probe is present in the electrolyte solution, Scheme 1A. The parallel elements (C_{dl} and $Z_W + R_{et}$) of the equivalent circuit are introduced since the total current through the working interface is the sum of distinct contributions from the Faradaic process, I_F, and the double-layer charging, I_C. Since all of the current must pass through the uncompensated resistance of the electrolyte solution, R_s, is inserted as a series element in the circuit. The two components of the electronic scheme, R_s and Z_W, represent bulk properties of the electrolyte solution and diffusion features of the redox probe in solution. Therefore, these parameters are not affected by chemical transformations occurring at the electrode surface. The other two components in the scheme, C_{dl} and R_{et}, depend on the dielectric and insulating features at the electrode/electrolyte interface. The double-layer capacitance depends on the dielectric permittivity introduced into the double-charged layer molecules, ε_{dl}, and for the less polar molecules the capacitance should be smaller, Equation 2, where $\varepsilon_o =$

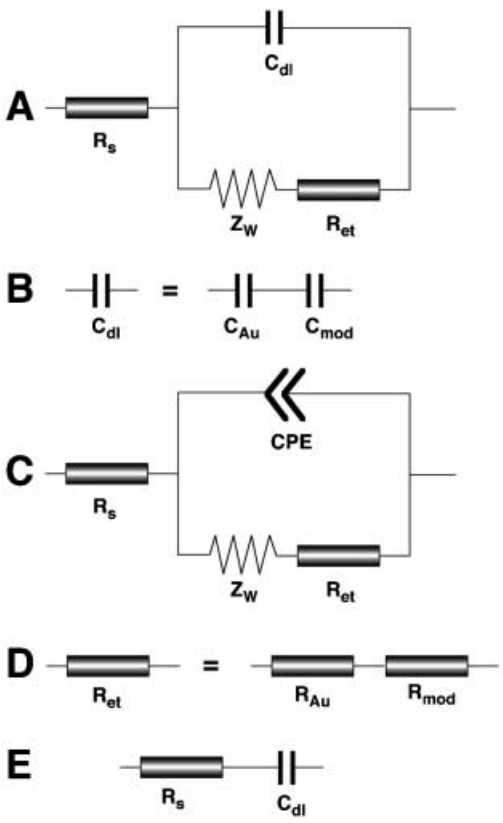

Scheme 1. A) General equivalent circuit for impedance spectroscopy measurements in an electrochemical cell. B) Equivalent circuit corresponding to the double-layer capacitance, C_{dl}, that includes the variable component, C_{mod}, controlled by the modifier layer. C) General equivalent circuit for the impedance spectroscopy with the constant phase element (CPE) depending on the roughness of the electrode surface. D) Equivalent circuit for the electron transfer resistance, R_{et}, that includes the variable component, R_{mod}, corresponding to the different modifier states. E) Equivalent circuit for non-Faradaic impedance spectroscopy measurements in the absence of the redox probe.

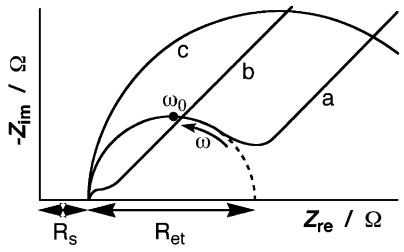

Scheme 2. Schematic Faradaic impedance spectra presented in the form of a Nyquist plot for: a) A modified electrode where the impedance is controlled by diffusion of the redox probe (low frequencies) and by the interfacial electron transfer (high frequencies). b) A modified electrode where the impedance is mainly controlled by diffusion of the redox probe. c) A modified electrode where the impedance is controlled by the interfacial electron transfer within the entire range of the applied frequencies. The arrow shows the direction of the frequency increase. Resistance of the electrolyte solution, R_s, and electron transfer resistance, R_{et}, are shown.

8.85×10^{-12} F m^{-1} is the dielectric constant of the vacuum, ε_ρ is the effective dielectric constant of the layer separating the ionic charges and the electrode surface, A is the electrode area, and δ is the thickness of the separating layer.

$$C_{dl} = \frac{\varepsilon_{dl} A}{\delta}; \quad \text{where } \varepsilon_{dl} = \varepsilon_o \varepsilon_\rho \tag{2}$$

In the equivalent electronic circuit the double-layer capacitance, C_{dl}, can be represented as a sum of a constant capacitance of an unmodified electrode (e.g., for a polycrystalline Au electrode, $C_{Au} \approx 40-60$ μF cm^{-2}, depending on the applied potential [42]) and a variable capacitance originating from the electrode surface modifier, C_{mod}, connected as series elements, Scheme 1B. Any electrode modifier of insulating features decreases the double-layer capacitance as compared to the pure metal electrode. Thus, the double-layer capacitance could be expressed by Equation 3.

$$\frac{1}{C_{dl}} = \frac{1}{C_{Au}} + \frac{1}{C_{mod}} \tag{3}$$

Sometimes, particularly when the electrode surface is rough [43], the electronic properties of the interface cannot be described sufficiently well with a capacitive element, and a constant phase element (CPE), Equation 4, should be introduced instead of C_{dl}, Scheme 1C.

$$\text{CPE} = A^{-1} (j\omega)^{-n} \tag{4}$$

The constant phase element reflects non-homogeneity of the layer, and the extent of the deviation from the Randles and Ershler model is controlled by the parameter n in Equation 4. Introduction of a CPE element into an equivalent electronic circuit instead of a simple capacitance element was shown to be important for the modeling of primary protein layers on an electrode surface, and the parameter n was found to be ca. 0.97 – 0.98 [44]. The CPE has meaning of capacitance and the coefficient A becomes equal to the C_{dl} when $n = 1$ [38, 39].

The electron transfer resistance, R_{et}, controls the electron transfer kinetics of the redox probe at the electrode interface. Thus, the insulating modifier on the electrode is expected to retard the interfacial electron transfer kinetics and to increase the electron transfer resistance. The electron transfer resistance at the electrode is given by Equation 5, where R_{Au} and R_{mod} are the constant electron transfer resistance of the unmodified electrode and the variable electron transfer resistance introduced by the modifier, in the presence of the solubilized redox probe, respectively. These resistances are also connected as series elements in the equivalent electronic circuit, Scheme 1D.

$$R_{et} = R_{Au} + R_{mod} \tag{5}$$

A typical shape of a Faradaic impedance spectrum (presented in the form of an impedance complex plane diagram – a Nyquist plot) includes a semicircle region lying on the -axis followed by a straight line, Scheme 2, curve a. The semicircle portion, observed at higher frequencies, corresponds to the electron transfer-limited process, whereas the linear part is characteristic of the lower frequencies range and represents the diffusionally limited electrochemical process. In the case of very fast electron transfer processes, the impedance spectrum could include only the linear part, curve b, whereas a very slow electron-transfer step results in a large semicircle region that is not accompanied by a straight line, curve c. The electron transfer kinetics and diffusional characteristics can be extracted from the spectra. The semicircle diameter equals to the electron transfer resistance, R_{et}. The intercept of the semicircle with the Z_{re}-axis at high frequencies ($\omega \to \infty$) is equal to the solution resistance, R_s. Extrapolation of the circle to lower frequencies yields an intercept corresponding to $R_s + R_{et}$. The characteristic frequency, ω_0, given by Equation 6, has the meaning of the reciprocal of the time constant of the equivalent circuit. The maximum value of the imaginary impedance in the semicircle part corresponds to $Z_{im} = 0.5R_{et}$ and is achieved at the characteristic frequency, ω_o.

$$\omega_o = (C_{dl} R_{et})^{-1} \tag{6}$$

One of the most important parameters governing the technique is the applied frequency. At low frequencies ($f < 1$ mHz) the impedance value is basically determined by the DC-conductivity of the electrolyte solution. At very high frequencies ($f > 100$ kHz) inductance of the electrochemical cell and connecting wires could contribute to the impedance spectra. Thus, the analytically meaningful impedance spectra are usually recorded at frequencies where they are mainly controlled by the interfacial properties of the modified electrodes (10 mHz $< f <$ 100 kHz).

The electron transfer resistance can be translated into the exchange current under equilibrium, I_o, Equation 7, and then the heterogeneous electron transfer rate constant, k_{et}, can be evaluated, Equation 8, where $R = 8.31$ J mol^{-1} K^{-1} is the gas constant, T is the temperature (K), $F = 9.65 \times 10^4$ C equiv^{-1} is the Faraday constant, A is the electrode area (cm^{-2}), [S] corresponds to the bulk concentration of the redox probe (mol cm^{-3}), and n is the number of electrons transferred per molecule of the redox probe.

$$R_{et} = RT\,(nFI_o)^{-1} \quad (7)$$

$$I_o = nFAk_{et}[S] \quad (8)$$

In the absence of any redox label in the electrolyte solution, only non-Faradaic impedance is operative. The electron transfer characterizing parameters, R_{et} and Z_W, become infinite, and the equivalent circuit can be simplified, as shown in Scheme 1E. The variable component in the circuit is presented by C_{mod}, and it affects the imaginary part of the impedance, Z_{im}, Equation 9, considering only the dense part of the double-charged layer.

$$Z_{im} = \frac{1}{\omega(C_{Au} + C_{mod})} \quad (9)$$

The experimental results can be analyzed graphically [38, 39] (in the case of Faradaic impedance spectra usually by the use of the Nyquist coordinates: Z_{im} vs. Z_{re}) in the frame of the theoretical model [40, 41]. A computer fitting of the experimental data to a theoretical model represented by an equivalent electronic circuit is usually performed. All electronic characteristics of the equivalent circuit and the corresponding physical parameters of the real electrochemical system can be extracted from such analysis. Since the variable parameters of the system represent the functions of the modifying layer and its composition, they can be used to quantitatively characterize the layer. Analysis of the $Z_{re}(\omega)$ and $Z_{im}(\omega)$ values observed at different frequencies allows the calculation of the following important parameters: a) the double-layer capacitance, C_{dl} and its variable component, C_{mod}; b) the electron transfer resistance, R_{et}, and its variable component, R_{mod}; c) the electron transfer rate constant, k_{et}, for the applied redox probe derived from the electron transfer resistance, R_{et}. Thus, the impedance spectroscopy represents not only a suitable transduction technique to follow the interfacial interactions of biomolecules, but it also provides a very powerful method for the characterization of the structural features of the sensing interface and for explaining mechanisms of chemical processes occurring at the electrode/solution interfaces [45].

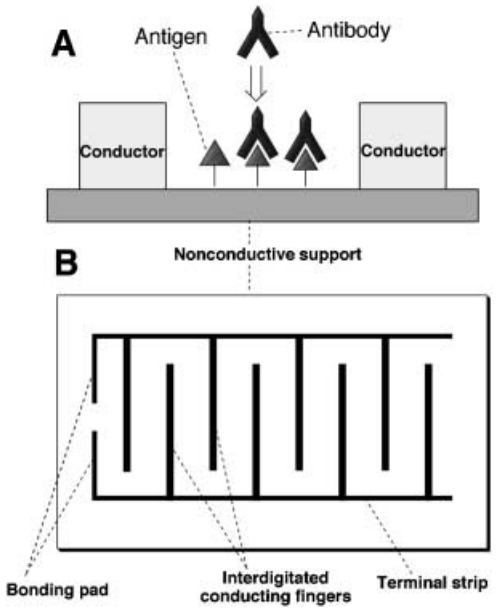

Scheme 3. A) Immunosensor for the in-plane impedance measurements between the conductive electrodes. B) Interdigitated electrode for the in-plane impedance immunosensing.

3. Immunosensors Based on Impedance Spectroscopy

Among the biomaterial-based sensing devices immunosensors are anticipated to be an important class of sensing systems in clinical diagnosis, food quality control, environmental analysis, detection of pathogens or toxins, and even the detection of explosives or drugs [46–48]. Several methodologies for the electrochemical transduction of the formation of antigen-antibody complexes on the electrode surface were reported [24, 49]. Impedance spectroscopy (including Faradaic impedance in the presence of a redox probe and non-Faradaic – capacitance measurements) represents an important electronic transduction means of antigen-antibody binding interactions on electronic elements.

3.1. Immunosensors Based on In-Plane Impedance Measurements Between Electrodes

In-plane impedance measurements were performed for analyzing antigen-antibody recognition processes. The detection path is based on the organization of two metallic conductive electrodes on an electrical insulator leaving a non-conductive gap between the electrodes, Scheme 3A. The gap was modified with a biomaterial capable of specific binding of a complementary unit, e.g., the gap was modified with antigen molecules for binding of the complementary antibody molecules, or an antibody was linked to the gap to bind the respective antigen molecules. Affinity binding of the respective complementary component results in the change of the electrical properties of the gap, thus affecting the impedance between the electrodes. The impedance changes can be measured as variation of conductivity, $\rho_{gap} = R_{gap}^{-1}$, between the electrodes, that represents changes in the real part, Z_{re}, of the complex impedance [50] or variation of

the gap capacitance, C_{gap}, that originates from the change of the imaginary part, Z_{im}, of the complex impedance [51]. In order to reach a high sensitivity, a short distance leaving a small dielectric gap between the conductors should separate the electrodes. For providing a large sensing surface on the thin gap, the conductive electrodes could be made as a pattern of interdigitated fingers [51], Scheme 3B. The applicability of nanoscale interdigitated electrodes for impedimetric sensing of the protein immobilization was studied and their potential use for immunosensing was addressed [52, 53].

For example, two copper conductors (25 μm high and 50 μm wide) were positioned on a surface of an insulating material, having a distance of 50 μm between them [51]. In order to observe capacitance changes for the gap, the conductors were insulated by a 1 μm layer of a non-conductive polymer that reduced the influence of Faradaic currents. A 0.3 μm layer of SiO_2 was vacuum deposited onto the polymer to provide suitable functional groups for the immobilization of a recognition element. Then antigen molecules were covalently bound to the gap surface via a silanization technique. When the functionalized sensing interface located in the gap between the electrodes was reacted with the complementary antibody units, the bulky protein molecules were bound to its surface replacing an aqueous solution. Due to the low dielectric constant of the antibody compared with water there was a change in the dielectric properties between the electrodes causing an alteration in the capacitance. A similar approach was used for detection of neurotransmitters and toxins [54], acetylcholine [55], alkaline phosphatase [56], and hIgG antibodies [57]. In order to amplify the dielectric changes resulting from the biorecognition event, bubbles of O_2 were generated in the sensing layer [58]. The sensing interface in the gap between the electrodes was functionalized with HIV antigens that were reacted with HIV antibodies. Then the sensing interface was reacted with anti-HIV-antibodies conjugated to the catalase enzyme. The enzyme stimulated the biocatalytic decomposition of added H_2O_2 yielding bubbles of O_2 in the sensing layer between the electrodes. This resulted in the significant decrease of the medium dielectric constant. The extent of the capacitance change in the system was dependent on the amount of oxygen bubbles generated by the biocatalytic process and thus related to the amount of the HIV antibodies bound to the sensing interface.

Antigen molecules labeled with conductive polymer chains were applied for the competitive analysis of antigens on an antibody-functionalized gap [59]. The impedance change of the system upon binding of the labeled antigen mainly originated from the conductivity increase between the electrodes, Scheme 4A. Polyaniline (**1**) was covalently bound to a rabbit IgG using glutaric dialdehyde as a linker, and then the functionalized IgG molecules were added to the gap functionalized with anti-rabbit goat IgG. This resulted in a significant increase in the conductivity between the electrodes measured at a fixed frequency of 20 kHz. Competitive immunoassay was performed in the presence of different concentrations of unlabelled IgG in the presence of a constant amount of the polyaniline-IgG conjugate. A decrease of the sensor response was observed as the concentration of unlabelled IgG increased, due to the decrease in the amount of the conductive IgG associated with the gap. The decrease of the system response was proportional to the IgG analyte concentration that could be sensed with a sensitivity limit that corresponded to 0.5 μg mL^{-1}. Another immunosensor was based on the conductance change of a phthalocyanine thin film assembled beneath the antigen-antibody sensing interface using the biocatalytic generation of iodine as a doping reagent of the phthalocyanine film [60], Scheme 4B. Horseradish peroxidase, HRP, was covalently bound to rabbit IgG. The HRP-labeled IgG was reacted with the sensing interface functionalized with anti-rabbit IgG, and then the bound HRP biocatalyzed oxidation of I^- ions to I_2 in the presence of H_2O_2. The film bridging the gap between the electrodes was composed of tetra-*tert*-butyl copper phthalocyanine (**2**) that revealed substantial decrease in the film resistance upon interaction with iodine (I_2). This allowed the direct sensing of the HRP-labeled IgG, as well as the sensing of unlabelled IgG using competitive assay.

A discontinuous ultra-thin metal film consisting of conductive metallic islands separated by nanosized gaps was placed between conductive electrodes and used for the impedimetric immunosensing of *Staphylococcus* enterotoxin B (SEB) [61, 62]. A Pt film was deposited on a silicon dioxide surface by electron beam evaporation at a rate of 0.1 Å s^{-1} resulting in a nominal thickness of 25 Å, as indicated by a quartz crystal microbalance analysis. Transmission electron microscopy images revealed that the film was composed of regularly distributed Pt islands of radii 30 to 60 Å, leaving uncoated silicon dioxide surface domains of 21 to 50 Å. The discontinuous metal film was further modified with a polysiloxane layer, which was used for the covalent coupling of anti-SEB antibodies. The impedance $|Z|$ spectra obtained for the anti-SEB-functionalized sensing layer in phosphate buffer shows the highest impedance value of ca. 1.8 kΩ at the frequency of 1×10^2 Hz, Figure 1A, curve a, that was approximately three orders of magnitude less than the impedance of the dry film. This suggests that the mechanism of electrical conductance through the Pt islands was dominated by ionic conductivity of the hydrated and buffered protein layer. The reaction of the anti-SEB-functionalized surface with the complementary SEB analyte resulted in a 98% decrease in the film impedance to the value of 25 Ω at 1×10^2 Hz, Figure 1A, curve b. The impedance decrease originates from the increase of the amount of the hydrated proteins between the conductive Pt islands. A calibration plot for the analysis of SEB was derived from the impedance spectra obtained at different concentrations of the toxin, Figure 1B.

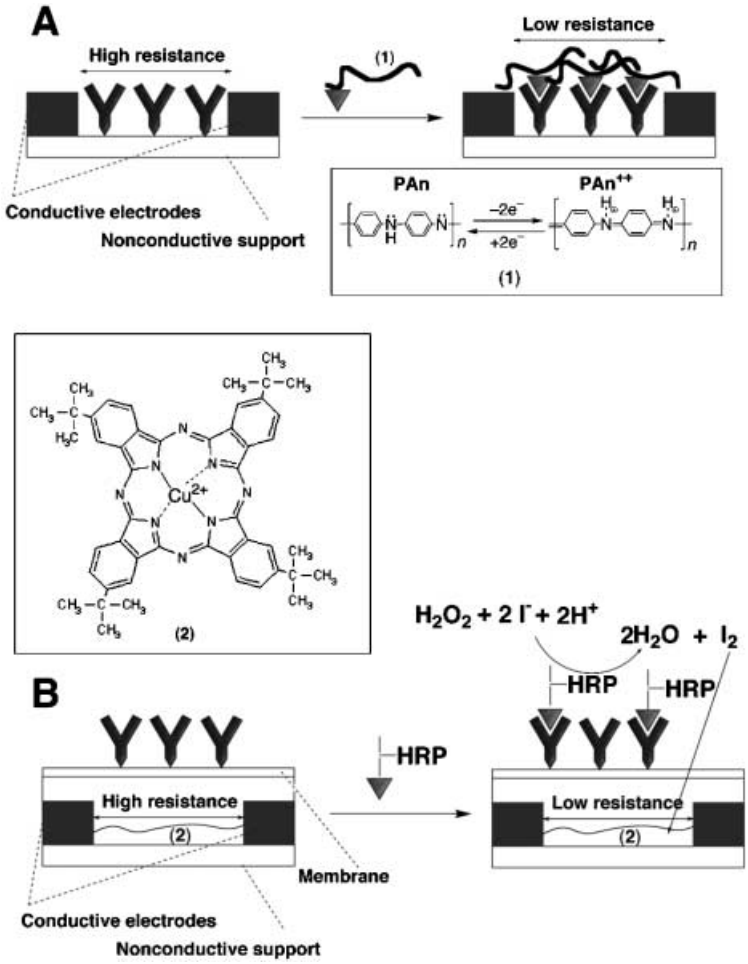

Scheme 4. Various mechanisms of the in-plane impedance immunosensing: A) The increase of the immunosensing film conductivity upon binding of the polyaniline-labeled IgG antigen to the anti-IgG antibody-functionalized membrane. B) The increase of the conductivity of the tetra-*tert*-butyl copper phthlocyanine (**2**) film upon I_2 generation by the immunosensing membrane in the presence of HRP-labeled antigen, H_2O_2 and iodide.

3.2. Immunosensors Based on Interfacial Impedance Measurements at Electrodes

Formation of antigen-antibody complexes on conductive supports yields a chemically modified film on the surface that alters the impedance features of the interface, Scheme 5. The formation of the antigen-antibody complex perturbs the double-charged layer existing at the electrode/electrolyte interface resulting in the increase of its thickness, δ_{dl}, and the insulation of the electrode surface in respect to redox labels added to the solution. This results in the capacitance change and electron transfer resistance change at the interface, respectively.

Various techniques were developed for the immobilization of the biorecognition components, antigens or antibodies, on electrode surfaces. For example, thin oxide layers existing on some electrode surfaces (e.g., indium-tin oxide electrode, Pt/Pt-OH electrode) provide hydroxyl groups for silanization and further covalent binding of antigens or antibodies [63], Scheme 6A. A versatile method for the organization of antigen-antibody monolayers on electrodes is based on the self-assembling of thiols on a gold electrode surface [64]. Thiol or disulfide groups were synthetically introduced into the antigen or antibody molecules in order to enable their direct tethering to Au electrodes [65–68]. For example, an epitope that consisted of amino acids 135–154 of the capsid protein VP1 of the foot-and-mouth-disease virus was used as a model antigen recognized by respective monoclonal and polyclonal antibodies [65, 66]. This synthetic polypeptide was covalently bound to ω-hydroxyundecanethiol, $HS(CH_2)_{11}OH$, using a succinic acid spacer and the synthetic antigen (**3**) was self-assembled at a Au electrode surface, Scheme 6B. Alternatively the biorecognition molecules could be chemically bound to a thiol monolayer pre-assembled at a Au electrode [69], e.g., using a cystamine self-assembled monolayer as a primary functionalized interface, Scheme 6C. A large variety of chemical coupling reactions was applied to covalently link antigen or antibody molecules to functional groups provided by self-assembled thiol monolayers [70]. Non-covalent affinity

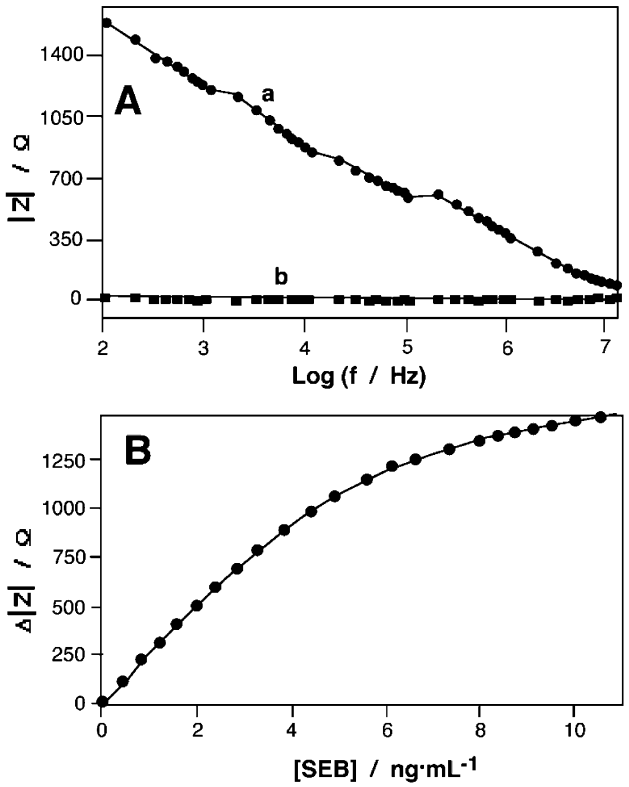

Fig. 1. In-plane impedance sensing of *Staphylococcus* enterotoxin B (SEB) on a discontinuous ultra-thin Pt film functionalized with anti-SEB antibodies: A) Absolute impedance value, $|Z|$, as a function of the applied frequency. Data recorded in: a) Phosphate buffer prior to the SEB binding, b) After the sensing film was exposed to the SEB solution, 100 ng mL^{-1}, for 1 hour. B) A calibration plot derived from the impedance measurements at the frequency of 100 Hz using different SEB concentrations. (Reproduced from [61] with permission).

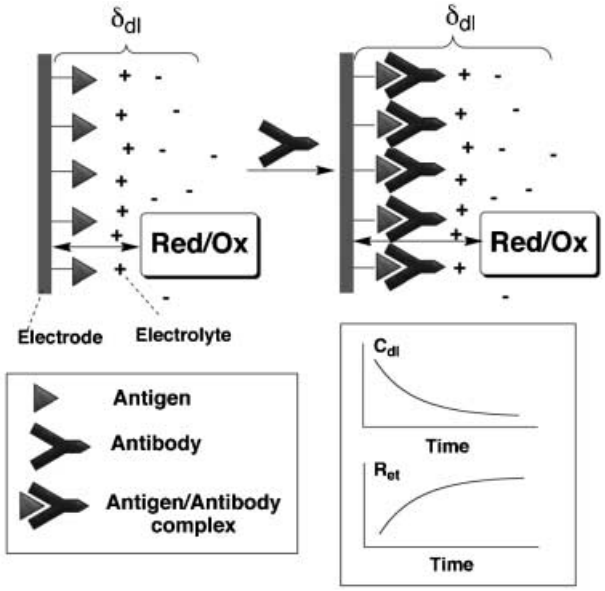

Scheme 5. Schematic illustration of interfacial impedance immunosensing: A bioaffinity interaction between an antibody and an antigen-functionalized electrode increases the double-charged layer thickness, δ_{dl}, and inhibits the interfacial electrochemical process of a redox probe. The electrode capacitance, C_{dl}, and the electron transfer resistance, R_{et}, are changed respectively.

binding of antibodies to an electrode surface has been exemplified with a biotinylated antibody (anti-human IgG) bound to a biotinylated polypyrrole layer through avidin linker [71], Scheme 6D. Direct visualization of IgG binding on different surfaces was achieved using AFM, and the results were compared with impedance spectra changes [72].

Impedance spectroscopy allows the detection of capacitance changes at the interfaces that originate from biorecognition events. These capacitance changes can be derived from the imaginary part, Z_{im}, of the complex impedance spectra. The interfacial capacitance can be measured at various biasing potentials (differential capacitance), thus allowing the electrical probing of the system when different charges exist at the electrode. Since antigens and antibodies are usually charged protein molecules, formation of the bioaffinity complexes between them could be affected by the charge applied onto the electrode surface. Furthermore, the orientation of the antigen/antibody complex vs. the electrode surface could be affected by the electrode charge. Therefore, capacitance changes observed upon formation of the bioaffinity complexes are potential dependent and the optimal conditions for their measurements could be found. Non-Faradaic impedance spectroscopy in the absence of a redox probe was applied to follow the biorecognition events at functionalized electrode surfaces. For example, Figure 2A,B, shows small changes of the absolute impedance value, $|Z|$, and the impedance imaginary part, Z_{im}, upon the association of the foot-and-mouth-disease virus antibody with a thiol monolayer functionalized with the synthetic polypeptide-antigen [66]. Although the impedance changes were small, they allowed the analysis of the kinetics of the antigen-antibody binding, Figure 2C. Similar capacitance measurements were applied for quantitative immunoanalysis [51]. For example, anti-rabbit IgG antibodies coupled to a self-assembled cystamine monolayer on a Au electrode were used for the detection of the respective antigen in a linear range between 0.5–8.5 ng mL^{-1} based on the analysis of capacitance changes by non-Faradaic impedance spectroscopy [73].

Faradaic impedance spectroscopy is usually considered to be more sensitive to the insulation of the electrode surface upon the binding of bulky antibodies to the antigen-functionalized electrode surfaces. In order to measure the full electrical impedance at the interface, including its real part, Z_{re}, a redox probe (often $[Fe(CN)_6]^{3-/4-}$ ions are used) is added to the electrolyte solution. The redox probe provides a Faradaic current at the electrode surface, if the appropriate potential is applied to the electrode (usually the electrode is biased at the standard potential, E°, of the redox probe). The changes in the real component of the impedance spectrum observed upon the bioaffinity complex formation at the electrode surface are usually higher than the respective capacitance changes, however, they are usually

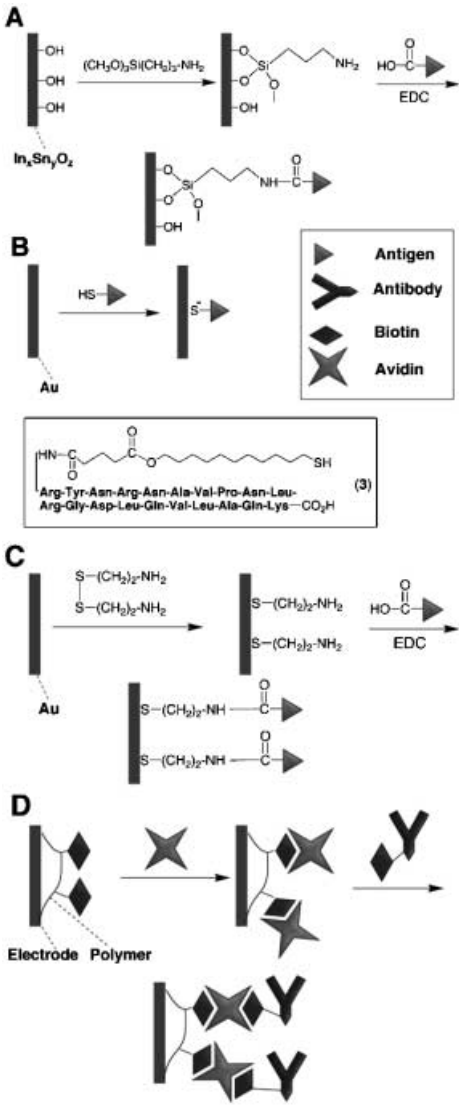

Scheme 6. Chemical functionalization of electrode surfaces with immunosensing components: A) Formation of a thin aminosiloxane film on a surface of a metal oxide electrode (e.g., indium-tin oxide) followed by carbodiimide coupling of an antigen (EDC = 1-ethyl-3-(3-dimethylaminopropyl)carbodiimide). B) Self-assembling of thiolated antigen molecules on a Au electrode surface (the exemplified antigen represents a thiolated oligopeptide (**3**) corresponding to an epitope of the foot-and-mouth-disease). C) Carbodiimide binding of an antigen to a self-assembled cystamine monolayer on a Au electrode. D) Affinity binding of a biotinylated antibody to a biotin-functionalized polymer film mediated by avidin units.

measured at a fixed potential. For example, interaction of a human mammary tumor associated glycoprotein with an electrode surface functionalized with its monoclonal antibody resulted in significant insulation of the electrode surface that was reflected by a large increase of the electron transfer resistance [74]. However, it should be noted that the changes in the Faradaic impedance spectrum upon the antigen-antibody complex formation are not always large. If the sensing layer is not well organized and contains many pinholes between the biomolecules, and the redox probe is sufficiently small to freely penetrate through these pinholes, the changes observed in the Faradaic impedance spectra could be minor. For example, Figure 3 shows a large increase in the electron transfer resistance, R_{et}, when a bare Au electrode was covered with an antigen-thiol monolayer, curve b, whereas a relatively small R_{et} increase was observed upon further binding of the antibodies to the antigen sensing monolayer, curve c, [65]. It has been shown that a mixed self-assembled monolayer composed of the antigen-functionalized thiols and non-derivatized thiols provides better binding of the antibody molecules because the antigen units are diluted and less screened by the neighbor units. Also in the mixed monolayer configuration the impedance measurements do not suffer from the penetration of the redox probe through pinholes between the antigen-antibody complex because they are blocked by the non-derivatized thiols. Another approach that allows minimizing the redox probe penetration through the pinholes includes the application of bulky redox molecules (e.g., NADH) or even redox enzymes [69]. For example, glucose oxidase (GOx) with tethered ferrocene units was used in the presence of glucose as a redox probe to sense the electrode surface blocking upon the antigen-antibody complex formation. Glucose oxidase tethered with ferrocene electron relays was electrically contacted at the electrode surface functionalized with small dinitrophehol (DNP)-antigen molecules, thus providing a bioelectrocatalytic current for glucose oxidation. However, when the large DNP-antibody molecules were associated with the electrode surface, the electrical contact between the GOx biocatalyst and the electrode was effectively blocked because the bulky biocatalyst cannot penetrate through small size pinholes in the antigen-antibody complex monolayer. This turns the Faradaic impedance spectra changes to be especially well observed [75, 76].

Redox polymers (e.g., polypyrrole) were used as sublayers for the immobilization of immunosensing units [77–80]. When the antigen-antibody binding proceeds atop of the redox polymer, the highly charged protein molecules appear at the interface. This results in the exchange of the counter ions between the redox polymer support and the protein layer that yields a significant change of the electrochemical properties of the polymer. Faradaic impedance spectroscopy was used to follow this change, thus allowing the impedimetric detection of the antigen-antibody complex formation. The mechanism of the process is, however, not well understood and the quantitative interpretation of the results is difficult.

Impedimetric immunosensors very often suffer from non-specific adsorption of biomolecules (e.g., proteins) accompanying the analyte [74]. Special attempts were made to minimize the non-specific adsorption phenomenon and its influence on the impedance measurements. These include special chemical treatment of the immunosensing electrodes, as well as development of special electrochemical cells and instruments. For example, bovine serum albumin (BSA) was co-immobilized in the immunosensing layer in order to decrease non-specific binding of proteins [65]. Dual-electro-

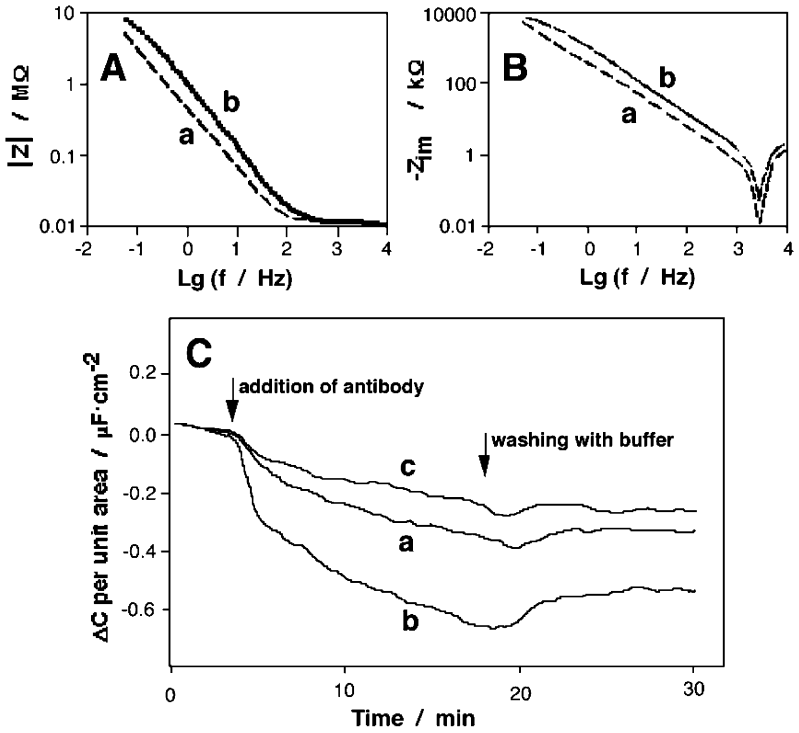

Fig. 2. Non-Faradaic impedance analysis of the foot-and-mouth-disease antibody on an electrode surface functionalized with the respective antigen (**3**). A) The absolute impedance value, $|Z|$, as a function of the applied frequency: a) Prior to the antibody binding, b) After the formation of the saturated antigen/antibody complex film. B) The imaginary part of the impedance, Z_{im}, as a function of the applied frequency: a) Prior to the antibody binding. b) After the formation of the saturated antigen/antibody complex film. C) The electrode capacitance changes upon the immunosensing: a) Using the antibody at a concentration of 1.74 mg mL^{-1}. b) Using the antibody at a concentration of 17.4 mg mL^{-1}. c) Using a non-specific antibody at a concentration of 17.5 mg mL^{-1}. (Reproduced from [66] with permission).

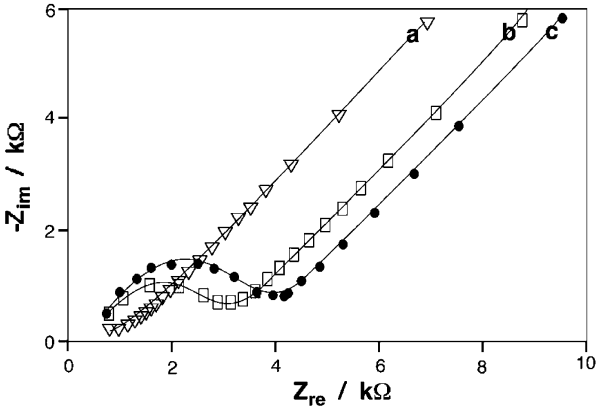

Fig. 3. Faradaic impedance spectra recorded upon sensing of foot-and-mouth-disease antibodies at a Au electrode functionalized with a self-assembled monolayer of the thiolated polypeptide (**3**) corresponding to the foot-and-mouth-disease antigen: a) Bare Au electrode. b) (**3**)-monolayer functionalized Au electrode prior to the reaction with the antibody. c) (**3**)-monolayer functionalized Au electrode after the reaction with the antibody. The data were recorded in the presence of $[Fe(CN)_6]^{3-/4-}$, 2 mM. (Reproduced from [65] with permission).

chemical flow cells were introduced to compare the impedance spectra in the two detection channels: with and without the analyte sample [63, 81]. Experimental [81] and theoretical [63] details on the use of differential impedance spectroscopy for immunosensing were discussed.

Another point that has been addressed is the often-observed poor reversibility of the immunological reactions. The binding between the antigen and the antibody is usually very strong. By applying acidic media or high concentration of salts or urea, the proteins associated with the antigen-antibody complex are unfolded, leading to separation of antigen and antibody. These severe conditions affect the protein that acts as the receptor component of the sensor and the reactivation of the sensing interface after separation of the antigen-antibody complex is often impossible. Even in the case, if the receptor component is not a protein and it has high chemical stability (e.g., dinitrophenyl antigen, DNP-antigen), the structure of the monolayer could be perturbed and the thiol anchor groups could be dissociated from the surface upon the conditions required for the affinity complex dissociation. Photoisomerizable antigen molecules were suggested as a means to tailor reversible and reusable immunosensor electrodes [75, 76, 82, 83], Scheme 7A. By this approach the antigen in photoisomer state **A** enables the sensing of the antibody by the electronic transduction of the

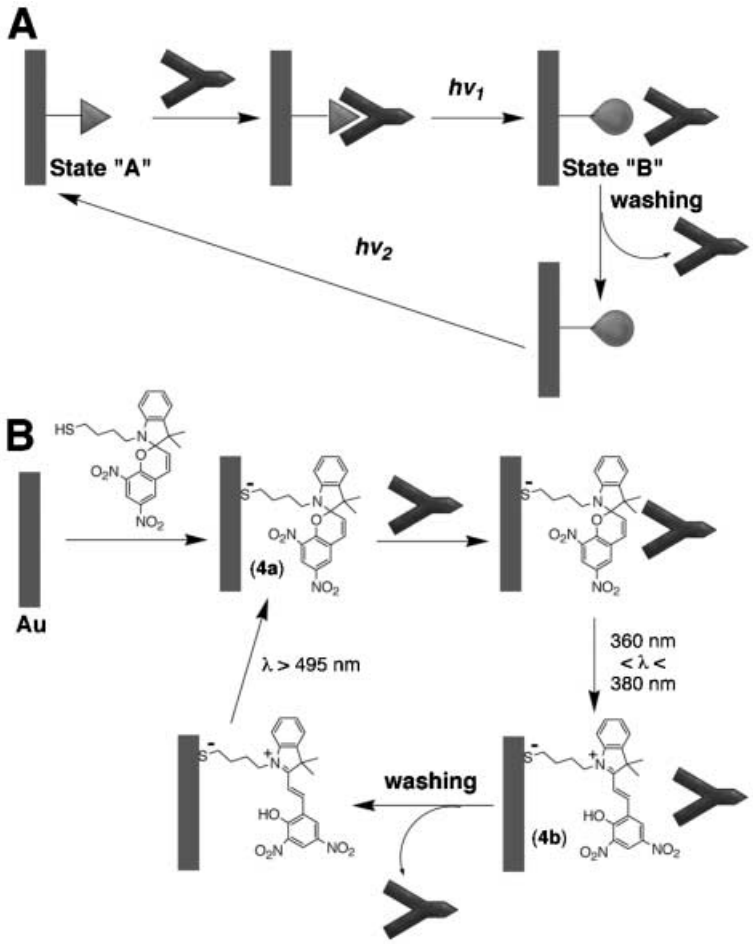

Scheme 7. Reversible immunosensing using a photoisomerizable antigen-monolayer-functionalized electrode: A) General scheme showing cyclic immunosensing upon an antibody binding-photoisomerization-washing off cyclic process. B) Assembly of the photoisomerizable dinitrospiropyran monolayer onto a Au electrode and its interaction with the DNP-antibody for reversible sensing of the DNP-Ab.

formation of the antigen-antibody complex at the transducer surface. Upon completion of the sensing process, the active sensing layer is photoisomerized to state **B.** The latter configuration lacks antigen features for the antibody binding and allows one to wash off the associated antibody. By further photoisomerization of the state **B** to the original photoisomer state **A**, the antigen layer is regenerated for a secondary sensing cycle. According to this concept a reversible immunosensor electrode for dinitrophenyl antibody, DNP-Ab, was assembled, Scheme 7B. A dinitrospiropyran (**4a**) photoisomerizable monolayer assembled onto a Au electrode acted as the active antigen interface for sensing DNP-Ab. Photoisomerization of the monolayer to the protonated dinitromerocyanine (**4b**) state generated an interface lacking antigen properties for the DNP-Ab. This allowed washing off the DNP-Ab, and by a subsequent photoisomerization of the monolayer to the dinitrospiropyran state, the active antigen interface was recycled. Figure 4 shows the Faradaic impedance spectra of the reversible immunosensing system in the different states measured in the presence of a negatively charged redox probe, $[Fe(CN)_6]^{3-/4-}$, [75]. The immunosensing was started by following the impedance features of the neutral dinitrospiropyran antigen (**4a**) monolayer-functionalized Au electrode, curve a. Association of the DNP-Ab with the antigen monolayer resulted in the increase of the electron transfer resistance, R_{et}, curve b, originating from the blocking of the electrode surface with the bulky DNP-Ab molecules. Photoisomerization of the dinitrospiropyran monolayer to the protonated dinitromerocyanine state (**4b**) and further washing off the DNP-Ab yields a positively charged monolayer that shows the smaller electron transfer resistance, curve c. It should be noted that R_{et} value observed for the positively charged dinitromerocyanine state is even smaller than the original R_{et} of the neutral dinitrospiropyran monolayer (**4a**). This is consistent with the fact that the negatively charged redox probe is electrostatically attracted by the positively charged state of the monolayer, resulting in the lower electron transfer resistance for this state. The next step in the process includes the photoisomerization of the dinitromerocyanine (**4b**) monolayer to the dinitrospiropyran monolayer (**4a**), curve a,

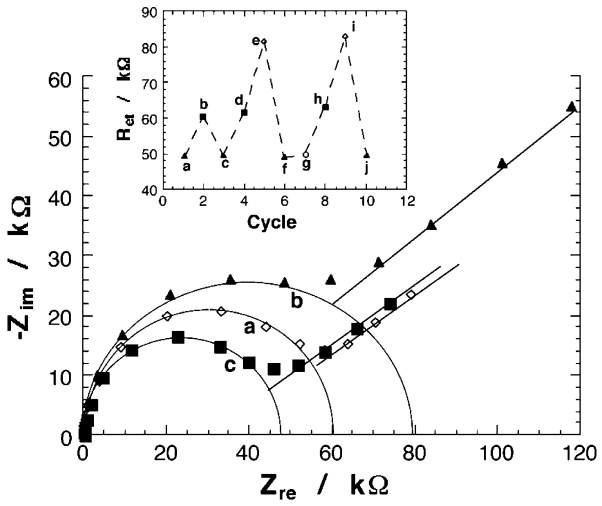

Fig. 4. Nyquist diagram (Z_{im} vs. Z_{re}) corresponding to the Faradaic impedance measurements at the photoisomerizable **4a**/**4b**-monolayer-modified Au electrode: a) **4a**-monolayer state. b) Affinity complex of DNP-Ab with the **4a**-monolayer. c) **4b**-monolayer state after washing off the DNP-Ab. Inset: Cyclic change of the electron transfer resistance, R_{et}, upon photoisomerization of the monolayer between **4a**/**4b** states, and association or dissociation of DNP-Ab to and from the monolayer interface: a and c) Monolayer in the **4b**-state. b and d) Monolayer in the **4a** state. e) **4a** monolayer state upon the addition of the DNP-Ab; f) Photoisomerization to **4b**-monolayer state and washing off the DNP-Ab; g) **4b**-monolayer upon the addition of DNP-Ab; h) Washing off the DNP-Ab followed by photoisomerization of the monolayer to the **4a** state; i) Addition of DNP-Ab to the **4a** monolayer; j) photoisomerization of the monolayer to **4b** state and washing off DNP-Ab. Impedance measurements were performed in the frequency range from 10 mHz to 20 kHz applying a constant bias potential, 0.6 V; amplitude of alternating voltage, 10 mV, using $[Fe(CN)_6]^{3-/4-}$, 1×10^{-2} M, as the redox probe in 0.01 M phosphate buffer, pH 7.0. (Reproduced from ref. 75 with permission).

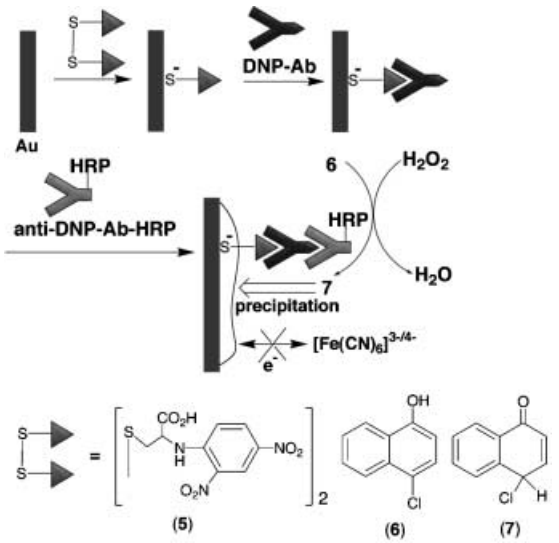

Scheme 8. Impedimetric immunosensing of the DNP-antibody on a DNP-self-assembled monolayer-functionalized Au electrode amplified by precipitation of an insoluble product biocatalyzed by anti-DNP-antibody-HRP conjugate bound to the primary sensing interface.

which is ready again to react with DNP-Ab. Thus, the reversible changes of the electron transfer resistance, $R_{et,}$ were derived from the real part, Z_{re}, of the Faradaic impedance spectra, Figure 4, inset. These changes reflect the association and dissociation of the antibody to and from the antigen monolayer, respectively, as well as the formation of different charges at the functionalized interface.

One of the major problems of impedimetric immunosensors is the relatively small change of the impedance spectra upon the direct binding of antibodies to the antigen-functionalized electrodes. The generated signals (i.e., the differences in the electron transfer resistance, ΔR_{et}, and in the double-charged layer capacitance, ΔC_{dl}) are especially insignificant when the antibody concentration is low and the surface coverage of the antigen-antibody complex is far from saturation. This major problem was addressed in recent studies directed to the development of amplified impedimetric immunosensors. In general, this approach includes the application of enzyme-labels bound to the components of the immunosensing system that perform biocatalytic reactions after the antigen-antibody recognition events in order to amplify the generated signal. It is similar to the ELISA immunosensing, but the process is performed at an electrode surface and the results are sensed by the Faradaic impedance spectroscopy. In order to increase the interfacial changes at the sensing interfaces and to amplify the resulting impedimetric signal, enzyme-labels that precipitate an insoluble product on the sensing interface were employed [44, 84–87]. This concept was exemplified with the sensing of DNP-antibody (DNP-Ab) at the electrode surface functionalized with a DNP-antigen self-assembled monolayer [44], Scheme 8. A DNP-antigen (**5**) monolayer was assembled onto the Au electrode surface. Challenging of the functionalized electrode with the complementary analyte-antibody, DNP-Ab, results in the formation of the antigen-antibody complex on the transducer. The extent of the complex formation is controlled by the concentration of the antibody in the analyzed sample and the time of interaction between the antigen-electrode and the antibody solution. Treatment of the resulting electrode with a probe-solution consisting of the anti-DNP-antibody-horseradish peroxidase conjugate (anti-DNP-Ab-HRP) yields the biocatalytically labeled antibody/anti-antibody complex on the surface. HRP biocatalizes the precipitation of an insoluble product (**7**) upon oxidation of 4-chloro-1-naphthol (**6**), and thus the formation of the precipitate (**7**) was used to probe the formation of the tri-component antigen/antibody/anti-antibody-HRP assembly on the electrode. Note that precipitation of **7** occurs only if the analyte antibody, DNP-Ab, binds to the support, and subsequently associates the anti-DNP-Ab-HRP probe. The amount of precipitate formed on the transducer is controlled by the surface concentration of the parent analyte antibody on the surface and the time-interval used for the biocatalyzed production of the insoluble film. That is, the amount of the

precipitate associated with the electrode surface relates to the concentration of the analyte-antibody in the sample. Furthermore, the generation of the insoluble film by the biocatalyzed process represents an amplification route for the formation of low coverage antigen-antibody complexes at the electrode surface. Substitution of the electrolyte solution with the protein molecules at the electrode surface and further increase of the thickness and density of the organic layer upon the biocatalytic precipitation process results in a significant change of the double-charged layer capacitance, C_{dl}, which is derived from the imaginary part, Z_{im}, of the impedance spectra. The decrease of the effective dielectric constant of the medium at the interface yields the respective decrease of C_{dl}. Figure 5A shows capacitance at the functionalized electrode upon the build-up of the antigen monolayer on the electrode, association of the DNP-Ab and the corresponding anti-DNP-Ab-HRP conjugate to the sensing surface, and upon the HRP-biocatalyzed precipitation of the insoluble product **7** on the electrode. The additional suppression of the interfacial capacitance upon the formation of the precipitate is evident. Nonetheless, the changes in real part of the impedance are expected to be substationally higher. The stepwise formation of the antibody and anti-antibody complexes on the electrode is anticipated to yield a hydrophobic layer on the electrode surface that perturbs the interfacial electron transfer processes between the electrode and a redox probe solubilized in the electrolyte solution. The barrier for the interfacial electron transfer should be amplified upon the precipitation of the insulating product on the electrode. This results in a significant change of the electron transfer resistance values, R_{et}, derived from the impedance spectra. Figure 5B shows the Faradaic impedance spectra of the DNP-antigen-functionalized electrode upon interaction with different concentrations of the analyte DNP-Ab, and amplification of the analysis of the DNP-Ab by means of the anti-DNP-Ab-HRP conjugate and the biocatalyzed precipitation of the insoluble product **7** for 12 minutes. As the concentration of the DNP-Ab is elevated, the electron transfer resistance, R_{et}, increases as a result of the formation of the insoluble film. Figure 5B, inset, shows the derived calibration plots that correspond to the R_{et} at the electrode before, curve a, and after amplification with the secondary anti-DNP-Ab-HRP conjugate and formation of **7**, curve b. A ca. 3-fold amplification of the immunosensing is evident upon comparison of the calibration plots with and without the formation of the precipitate, curves b and a, respectively. The electron transfer resistance increases, as the concentration of DNP-Ab is elevated, and then levels-off to a constant value at higher concentrations of DNP-Ab. These results are consistent with the fact that the DNP-antigen monolayer is saturated with the DNP-Ab at higher concentrations of the analyte-antibody. This results in the saturation of the electrode surface with the biocatalytic conjugate, and the formation of a saturation amount of the precipitant on the electrode.

The extent of the signal amplification is controlled by the time-interval for the precipitation of the insoluble product.

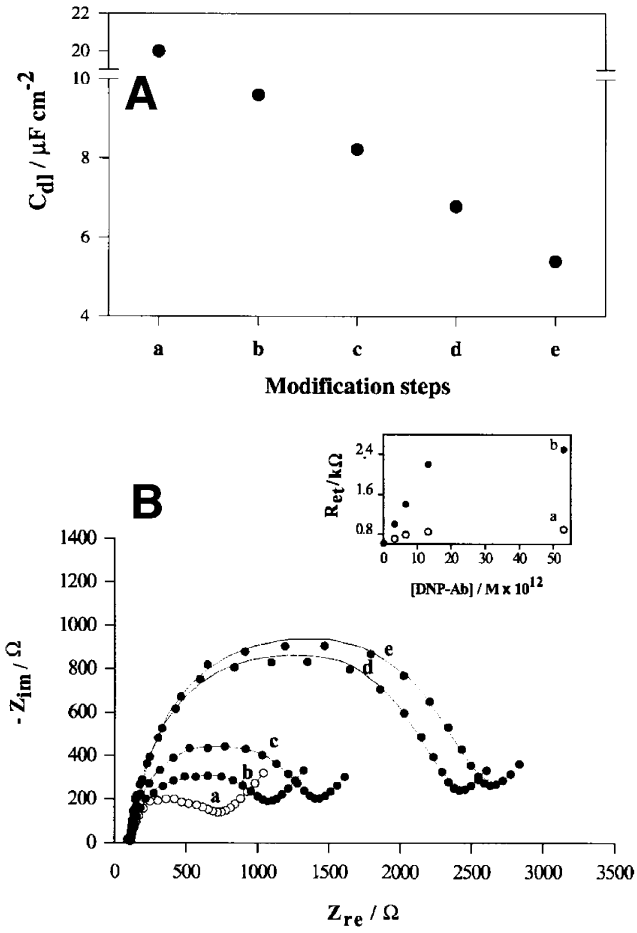

Fig. 5. Non-Faradaic and Faradaic impedimetric sensing of the DNP-Ab amplified by the precipitation of the insoluble product. A) Double-layer capacitance, C_{dl}, at the electrode upon the stepwise assembly of: a) the bare Au electrode. b) The DNP-antigen monolayer electrode. c) The DNP-antigen/DNP-Ab layered assembly. d) DNP-antigen/DNP-Ab/anti-DNP-Ab-HRP layered assembly. e) After the biocatalyzed precipitation of the insoluble product **7** on the electrode. B) Nyquist diagrams (Z_{im} vs. Z_{re}) for the Faradaic impedance measurements corresponding to the sensing of variable concentrations of the DNP-Ab amplified by biocatalyzed precipitation of the insoluble product (**7**). The DNP-antigen monolayer electrodes were treated with different concentrations of the DNP-Ab for 5 minutes. The resulting electrodes were then treated with the anti-DNP-Ab-HRP conjugate, 10 μg mL^{-1}, for 5 minutes, and the electrodes were then allowed to stimulate the biocatalyzed precipitation of **7**; $[H_2O_2] =$ 30 mM, $[\mathbf{6}] = 1$ mM. Impedance spectra corresponding to the DNP-antigen-functionalized electrode (a) and to the primary interaction of the DNP-antigen monolayer with the DNP-Ab at concentrations of: b) 0.5 ng mL^{-1}; c) 1 ng mL^{-1}; d) 2 ng mL^{-1}; e) 8 ng mL^{-1}. Inset: Calibration plots corresponding to the electron transfer resistances at the DNP-antigen monolayer-functionalized electrodes upon the analysis of different concentrations of the DNP-Ab: a) R_{et} observed by the direct interaction of the DNP-Ab with the sensing interface, b) R_{et} observed by the amplification of the initial binding of the DNP-Ab with the biocatalyzed precipitation of **7.** Impedance measurements were performed in the frequency range from 10 mHz to 20 kHz applying a constant bias potential, 0.17 V; amplitude of alternating voltage, 10 mV, using $[Fe(CN)_6]^{3-/4-}$, 1×10^{-2} M, as the redox probe in 0.01 M phosphate buffer, pH 7.0. (Reproduced from [44] with permission).

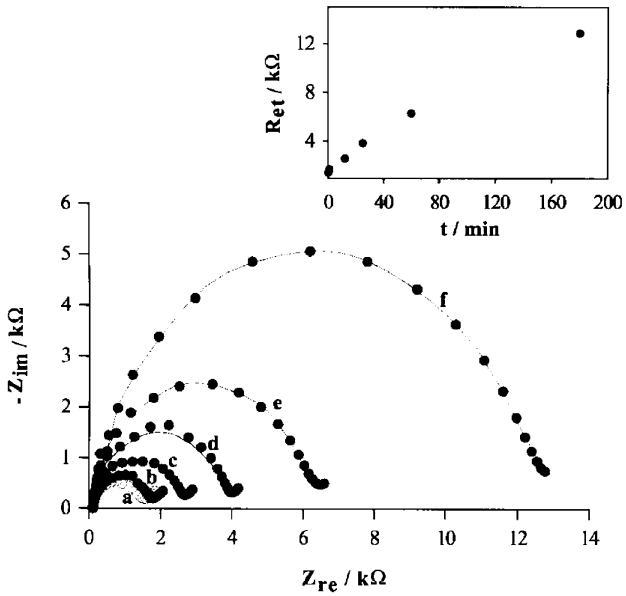

Fig. 6. Nyquist diagrams (Z_{im} vs. Z_{re}) corresponding to the Faradaic impedance spectra observed upon the time-dependent precipitation of the insoluble product **7.** The DNP-antigen monolayer electrode was treated with the DNP-Ab, 2 ng mL^{-1}, for 5 minutes, and then interacted with the anti-DNP-Ab-HRP conjugate, 10 μg mL^{-1}, for 5 minutes: a) Prior to the precipitation, b) 1 minute of precipitation, c) 12 minutes of precipitation, d) 40 minutes of precipitation, e) 60 minutes of precipitation, f) 180 minutes of precipitation. Inset: Electron transfer resistances as a function of time upon analysis of the DNP-Ab. Data extracted from the Nyquist plots. The experimental conditions were similar to those in Figure 5. (Reproduced from [44] with permission).

Figure 6 shows the effect of the time-interval used for the precipitation of the insulating layer on the interfacial electron transfer resistances. In this experiment, the DNP-antigen monolayer electrode was treated with a constant concentration of the analyte DNP-Ab, corresponding to 2 ng mL^{-1}, and the biocatalyzed precipitation of **7** onto the electrode was allowed to proceed for different time-intervals. The semicircle diameters of the respective Faradaic impedance spectra increase as the biocatalyzed precipitation of **7** occurs for longer time-intervals. For example, the electron transfer resistances at the electrode surface after 12 and 180 minutes of biocatalytic precipitation correspond to $R_{et} = 2.6$ kΩ and 12.9 kΩ, respectively. That is, as the biocatalyzed precipitation of **7** yields thicker insulating layers on the electrode, the interfacial electron transfer resistances are enhanced. Figure 6, inset, shows the plot of the R_{et} as precipitation proceeds with time. It is evident that the electron transfer resistance tends to reach a saturation value. This saturation value of R_{et} is reached when the insoluble film insulates the biocatalyst from the substrate that blocks further precipitation of **7**.

A similar approach was used for the impedimetric detection of whole cells of *E. coli* bacteria [88]. The primary affinity binding of the *E. coli* cells to the electrode surface functionalized with an *E. coli*-antibody was detected by the

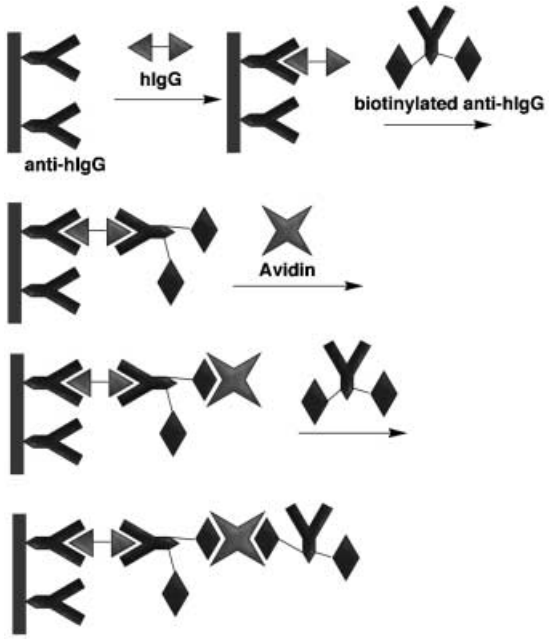

Scheme 9. Assembly of an extended protein multilayer system for the impedimetric immunosensing: The primary binding of the analyte hIgG antigens to the sensing interface functionalized with anti-hIgG antibodies is amplified by the secondary stepwise binding of the biotinylated anti-hIgG and avidin.

Faradaic impedance measurements. The recognition process was further amplified by the coupling of the *E. coli*-antibody-alkaline phosphatase conjugate to the surface that stimulated the precipitation of an insoluble material onto the electrode surface. This impedimetric immunosensor allowed analysis of the *E. coli* cells with the detection limit of 6×10^3 cells mL^{-1}. A linear response in the electron transfer resistance for the analysis of the *E. coli* cells was found within the range of 6×10^4 to 6×10^7 cells mL^{-1}.

Alternatively, the impedimetric immunosensing could be amplified by building of an extended network of non-catalytic but very bulky protein molecules after the primary recognition event. For example, an electrode functionalized with anti-human IgG antibodies (anti-hIgG) was reacted with the analyte hIgG antigens [89], Scheme 9. After the primary recognition event, the sensing interface was further reacted with biotinylated anti-hIgG and then several steps of the reactions with avidin and a biotinylated protein were performed, resulting in the formation of extended multilayer of proteins on the electrode surface. The multilayer density relates to the coverage of the sensing surface with the primary analyte-antigen, but the formation of the thicker isolating layer results in the amplification of the impedimetric signal, Figure 7.

An interesting approach for the amplified impedimetric analysis of antigen-antibody interactions has involved the insulation of the electrode with extended array of liposomes [90] or functionalized liposomes that include a biocatalyst which precipitates an insoluble product on the transducer [86]. In the latter system, dual amplification is achieved by

the primary insulation of the electrode interface with the liposomes, and the secondary hydrophobic blocking of the electrode surface with enzyme-generated insoluble product. This method was applied for the impedimetric analysis of the cholera toxin [86], Scheme 10. A Au electrode was primarily modified with protein G that allowed binding of the anti-cholera-toxin antibody, which represents the sensing component for the analysis of cholera toxin. After the sensing event (binding of the cholera toxin to the anti-cholera-toxin antibody) the electrode surface was reacted with liposomes derivatized with ganglioside GM1 and HRP. The ganglioside GM1 units bind to the cholera toxin and result in the association of the liposomes to the sensing interface. The insulation of the electrode surface by the liposomes perturbs the interfacial impedance features of the electrode and provides the primary amplification path. The HRP-mediated oxidation of 4-chloronaphthol (**6**) to the insoluble product (**7**) provides the secondary amplification route, since the precipitation alters the interfacial electron transfer resistance and capacitance of the electrode. Figure 8 shows the amplified impedimetric analysis of cholera toxin. It is evident that elevation of the cholera toxin concentration results in the increase of the electron transfer resistance in the respective Faradaic impedance spectra. The dual amplification process allows the impedimetric analysis of cholera toxin with the low detection limit equal to ca. 1×10^{-13} M, Figure 8, inset.

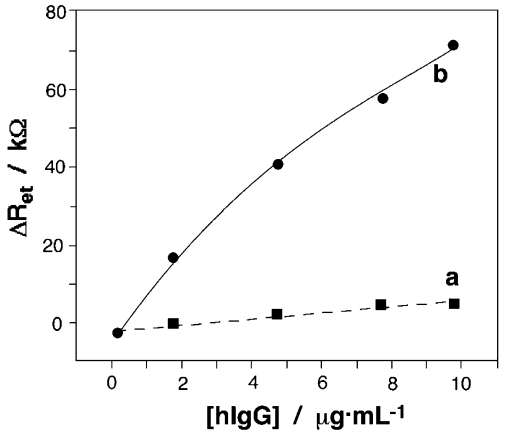

Fig. 7. The changes of the electron transfer resistance, R_{et}, derived from the respective Faradaic impedance spectra upon the sensing of hIgG at the anti-hIgG antibody-functionalized electrode: a) Without amplification. b) After amplification by the stepwise binding of the biotinylated anti-hIgG and avidin. (Reproduced from [89] with permission).

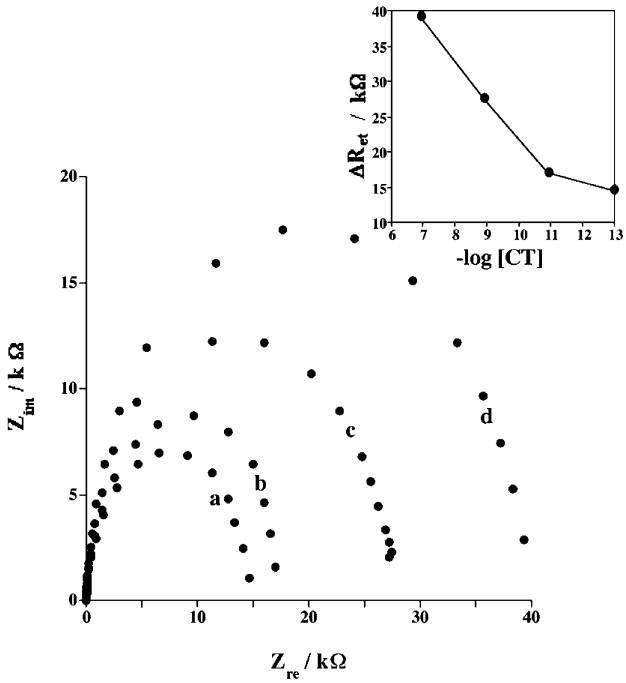

Fig. 8. Faradaic impedance spectra corresponding to the amplified analysis of different concentrations of the cholera toxin (CT) by the biocatalyzed precipitation of **7**: a) 1×10^{-7} M of CT, b) 1×10^{-11} M of CT, c) 1×10^{-9} M of CT, and d) 1×10^{-13} M of CT. Inset: Calbration plot corresponding to the changes in the electron transfer resistance at the electrode upon the amplified sensing of different concentrations of the CT.

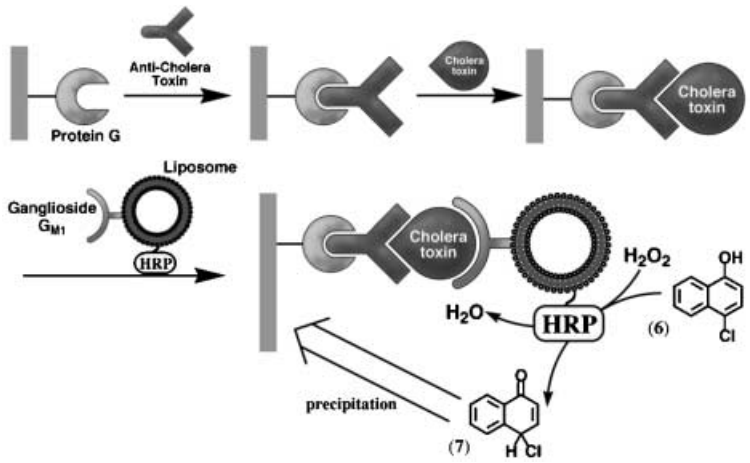

Scheme 10. Amplified sensing of the cholera toxin using a GM1-tagged HRP-functionalized liposome and the biocatalyzed precipitation of the insoluble product.

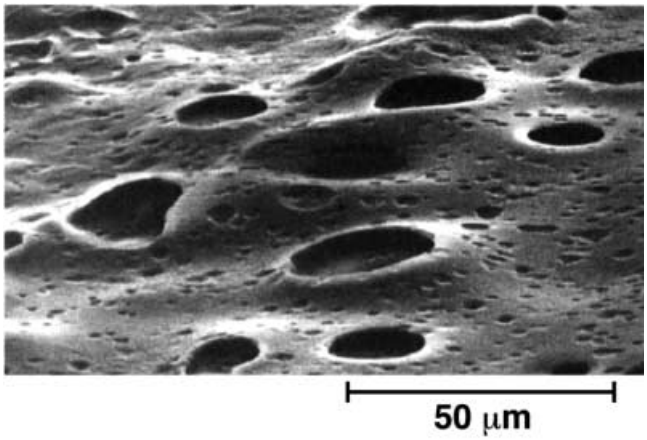

Fig. 9. Electron micrograph of a polymer (Eudragit S 100)-coated electrode after the partial breakdown due to the enzymatic reaction coupled to the antigen-antibody binding on the sensing interface. (Reproduced from [91] with permission).

Another amplification route includes enzyme-catalyzed polymer dissolution on the sensing interface [91, 92]. This process results in the decrease of the electron transfer resistance at the sensing interface that is opposite to the formation of the precipitant, which yields the higher electron transfer resistance. According to this method, the immunosensing system was organized on a top of an organic polymer membrane. After the primary binding of an analyte-antibody to the antigen-functionalized surface, the secondary antibody labeled with a hydrolytic enzyme was attached to the surface, and the hydrolytic breakdown of the polymer support was biocatalyzed. Figure 9 shows an electron micrograph of the polymer layer with pores generated upon the biocatalytic reaction. These pores provide penetration of the redox probe through the membrane that decreases the impedance value. The extent of this impedance decrease relates to the amount of the bound secondary antibody – hydrolytic enzyme conjugate that is proportional to the primary antigen-analyte antibody complex loading on the sensing surface.

4. DNA Sensors Based on Impedance Spectroscopy

The development of DNA-sensor devices [93 – 95] attracts substantial research efforts directed to gene analysis, detection of genetic disorders, tissue matching, and forensic applications [96 – 99]. The electronic transduction of the formation of nucleic acid/DNA complexes on electronic transducers such as electrodes or semiconductors could provide quantitative information on the DNA-analyte in the sample [94]. The design of bioelectronic DNA-sensing devices requires the development of analytical routes that address two basic goals: i) The detection of DNA should reveal high sensitivity and eliminate the need for pre-amplification of the DNA content in the sample by the polymerase chain reaction (PCR). For this purpose, chemical and physical amplification means need to be included into the analytical protocols. ii) The detection paths should reveal high specificity and selectivity for the analysis of mutants in the sample. Ideally, analysis schemes for the detection of single base mismatches are required.

The development of biochemical DNA-sensors requires the immobilization of nucleic acids, acting as the sensing interface, on the electronic transducers and the electronic transduction of the hybridization occurring with the analyte DNA on the transducer. As the nucleic acids and the resulting nucleic acid/DNA complexes are oligoanionic polymers, their immobilization on surfaces generates a negatively charged interface that repels negatively charged redox labels, and particularly multi-charged negative ions such as $[Fe(CN)_6]^{3-/4-}$. The repulsion of the redox label is anticipated to inhibit the interfacial electron transfer and thus leads to enhanced electron transfer resistance, R_{et}. Thus, Faradaic impedance spectroscopy seems to be an effective means to follow the adsorption and assembly of nucleic acids on conductive surfaces, and to characterize DNA hybridization processes on the transducers. Indeed, the adsorption of nucleotides [100 – 102] and oligonucleotides [103 – 107] on different electrode surfaces were studied by Faradaic impedance spectroscopy. For example, Figure 10 shows the gradual increase of the interfacial electron transfer resistance, R_{et}, at a Au electrode upon the time-dependent assembly of the thiolated nucleic acid, 5′-TCTATCCTACGCT-$(CH_2)_6$-SH-3′, using $[Fe(CN)_6]^{3-/4-}$ as the redox label for probing the generation of the thiolated nucleic acid monolayer [108]. The increase in the R_{et} value upon the build-up of the nucleic acid monolayer was attributed to the enhanced repulsion of the $[Fe(CN)_6]^{3-/4-}$ by the negatively charged interface. Using chronocoulometric and quartz-crystal microbalance measurements the time-dependent surface coverage of the analyzed nucleic acid could be assayed and the interfacial electron transfer resistance could be correlated with the coverage of the nucleic acid. For example, at surface coverage of ca. 8×10^{-11} mol cm^{-2} the interfacial electron transfer resistance corresponded to $R_{et} = 5.3$ kΩ. Figure 10, inset, shows gradual increase of the DNA surface coverage upon self-assembling of the thiolated DNA on the Au electrode surface.

The modification of surfaces with different DNA-composites such as DNA-carbon nanotubes [109] or oligocationic polymer-DNA layer-by-layer deposited films [110, 111] were studied by Faradaic impedance spectroscopy. For example, the interfacial electron transfer resistance of layer-by-layer deposited films consisting of the cationic polymer, poly(dimethyldiallylammonum chloride), and DNA was found to be controlled by the number of layers associated with the electrode. Figure 11A shows the impedance spectra of the deposited films that include increasing numbers of the polymer-DNA bilayers (the DNA is always the outer interface). Figure 11B shows that the interfacial electron transfer resistance ($[Fe(CN)_6]^{3-/4-}$ as redox-label) increases with the number of layers. It was also demonstrated that the association of small organic molecules (e.g., drugs) with DNA adsorbed on electrodes could affect the impedance

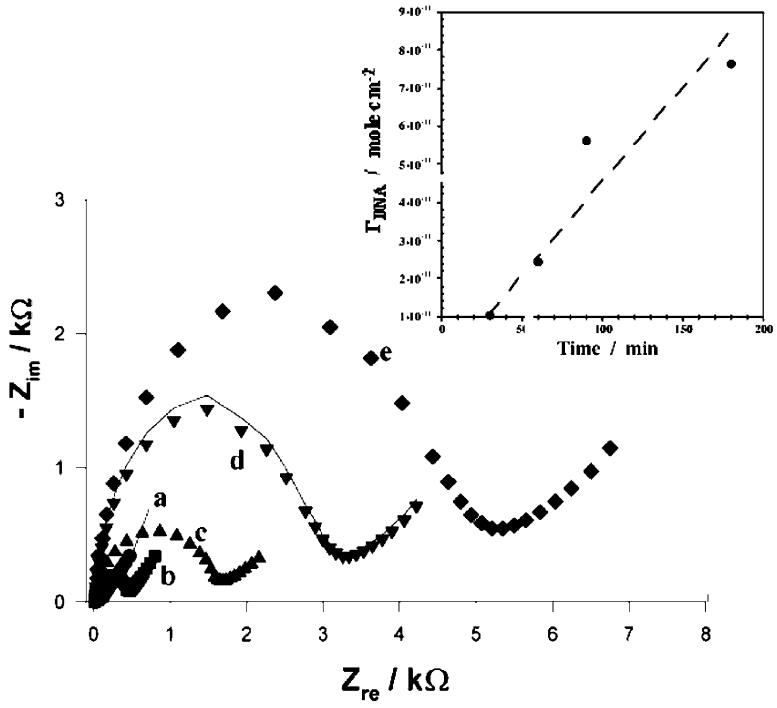

Fig. 10. Faradaic impedance spectra of: a) A bare Au electrode and (b, c, d, and e) after modification of the Au electrode with thiolated oligonucleotide, 5′-TCTATCCTACGCT-$(CH_2)_6$-SH-3′, 5 μM, for 30, 60, 90, and 180 minutes, respectively. Impedance measurements were performed in the frequency range from 10 mHz to 20 kHz applying a constant bias potential, 0.17 V; amplitude of alternating voltage, 10 mV, using $[Fe(CN)_6]^{3-/4-}$, 1×10^{-2} M, as the redox probe in 0.01 M phosphate buffer, pH 7.0. Inset: Time-dependent increase of the DNA coverage on the Au electrode upon self-assembling of the thiolated DNA derived from the complementary microgravimetric measurements.

spectrum of the interface and thus impedance spectroscopy was applied to characterize the binding of these molecules to DNA [112–115].

The dependence of the interfacial electron transfer resistance and capacitance features of DNA-modified electrodes on the amount of the oligonucleic acids at the interface allows the use of Faradaic impedance spectroscopy as a versatile tool to amplified electronic detection of DNA [90, 116–119]. The analysis of single-base mismatches in DNA [108, 120] and the characterization of biocatalyzed transformations on DNA (or RNA) associated with electrodes (e.g., replication, scission, ligation) were accomplished by Faradaic impedance spectroscopy [121, 122].

4.1. Impedimetric Sensing of DNA Hybridization

The analysis of a target DNA is based on its hybridization with a complementary nucleic acid on the electronic transducer [123]. The fact that the analyte DNA is an oligonucleonic polyelectrolyte suggests that formation of the nucleic acid/DNA complex on an electrode surface would generate a negatively charged interface that electrostatically repels an anionic redox probe such as $[Fe(CN)_6]^{3-/4-}$. The electrostatic repulsion of the redox probe from the electrode introduces a barrier for electron transfer at the electrode support, thus turning impedance spectroscopy as an ideal method to probe DNA hybridization at electrodes [116, 124]. That is, in the presence of an anionic redox probe, the DNA hybridization with a nucleic acid-functionalized electrode will be accompanied by an increase in the interfacial electron transfer resistance, R_{et}, that will be reflected in the Z_{re} component of the impedance spectrum.

A model system that involves the amplified impedimetric detection of the mutant characteristic to the Tay-Sachs (TS) genetic disorder was reported [116]. The nucleic acid primer (**8**) was assembled onto a Au electrode surface, using a five-base thiophosphate-T tag in the oligonucleotide as an anchoring group, Scheme 11A. The 13-mer oligonucleotide (**8**) included a 12-base sequence that is complementary to a part of the TS mutant (**9**). The resulting **8**-functionalized electrode was interacted with the TS-mutant. Figure 12 shows the impedance features presented as Nyquist plots of the bare Au electrode, curve a, the **8**-functionalized electrode, curve b, and the functionalized electrode after treatment with the complementary mutant (**9**), curve c, in the presence of $[Fe(CN)_6]^{3-/4-}$ as the redox probe. Significant differences in the impedance spectra were observed upon the stepwise formation of the double-stranded (ds)-oligonucleotide (**8**/**9**) complex. The respective electron transfer resistances, R_{et}, were derived from the semicircle diameters of the impedance spectra: R_{et} for the bare Au electrode was ca. 60 Ω and it increased to ca. 80 Ω and ca. 105 Ω upon functionalization of the surface with **8** and

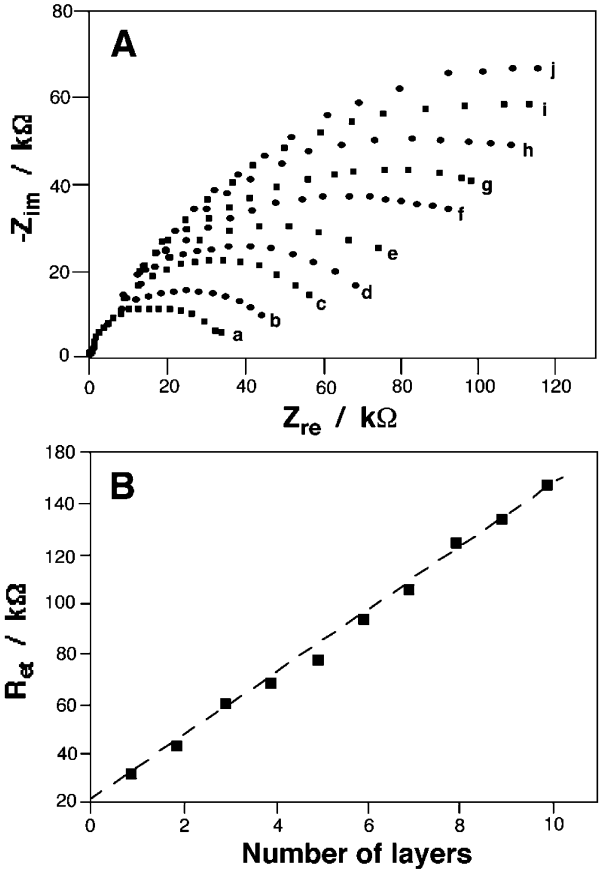

Fig. 11. Faradaic impedance spectroscopy of the layered polyelectrolyte/DNA assemblies: A) Nyquist diagrams (Z_{im} vs. Z_{re}) of the Faradaic impedance spectra corresponding to layer-by-layer deposition of poly(dimethylammonium chloride) and calf thymus DNA: a–j) correspond to 1–10 layers of the polymer/DNA (DNA layer was always the outer layer). B) The electron transfer resistances, R_{et}, derived from the Faradaic impedance spectra of the polymer/DNA layered systems. (Reproduced from [110] with permission).

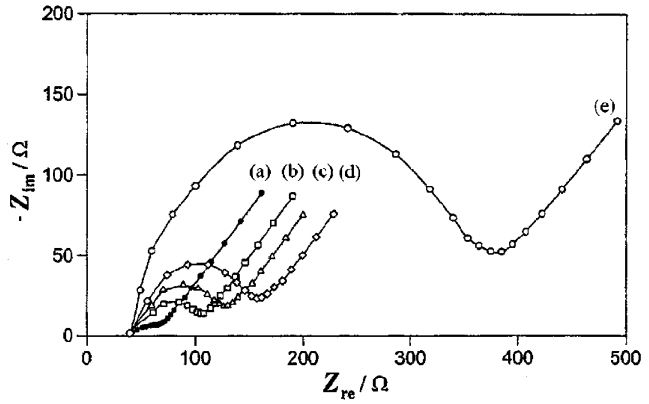

Fig. 12. Nyquist diagrams (Z_{im} vs. Z_{re}) for the Faradaic impedance sensing of the DNA hybridization amplified by the secondary hybridization with a biotinylated oligonucleotide followed by avidin binding: a) The bare Au electrode. b) The DNA probe (**8**)-functionalized Au electrode. c) The (**8**)-functionalized Au electrode after 30 minutes of incubation with the DNA analyte (**9**), 30 ng mL^{-1}. d) The ds-DNA complex (**8**/**9**) after 30 minutes of incubation with the biotinylated-oligonucleotide (**10**), 40 ng mL^{-1}. e) After10 minutes of incubation with avidin, 5 ng mL^{-1}. The impedance spectra were recorded within the frequency range 0.1 Hz–50 kHz at the bias potential, 0.17 V; amplitude of alternating voltage, 5 mV, using $[Fe(CN)_6]^{3-/4-}$, 1×10^{-2} M, as the redox probe in 0.01 M phosphate buffer, pH 7.0. (Reproduced from [116] with permission).

further formation of the ds-oligonucleotide complex with **9.** This is consistent with the fact that the negatively charged interface, formed upon the assembly of **8** on the electrode, repels the negatively charged redox probe. This introduces a barrier for interfacial electron transfer and results in the increased electron transfer resistance. Formation of the ds-oligonucleotide complex (**8**/**9**) enhances the repulsion of the redox probe and results in a further increase in the electron transfer resistance at the electrode. In order to confirm and amplify the formation of the ds-oligonucleotide complex, the sensing interface was interacted with the biotinylated oligonucleotide (**10**), Scheme 11A. The latter oligonucleotide was complementary to the residual sequence of the analyte DNA that was left non-hybridized in the previous modification step. The hybridization process between the **8**/**9** complex and **10** results in further increase of the electron transfer resistance ($R_{et} = 134\ \Omega$) in the impedance spectrum, Figure 12, curve d, that confirms the formation of **8**/**9** complex in the previous step and amplifies the signal. As the oligonucleotide **10** is labeled by biotin, the subsequent reaction of the oligonucleotide **8**/**9**/**10** superstructure with avidin is anticipated to further inhibit the electron transfer due to the hydrophobic insulation of the sensing interface. Figure 12, curve e shows the impedance spectra after the reaction of the sensing interface with avidin, demonstrating a substantial increase in the diameter of the semicircle domain, which translates to $R_{et} = 340\ \Omega$. The last amplification step allowed the analysis of the oligonucleotide **9** with the detection limit of 3.5×10^{-12} mol mL^{-1}. A control experiment demonstrated that the oligonucleotide **9a**, which includes the normal gene sequence, does not bind to the 8-functionalized interface and, therefore, does not result in the impedance spectrum change. Thus, the impedimetric method allowed discrimination between the mutant **9** and normal **9a** gene sequence and provided the amplified analysis of **9** with a low detection limit.

Additional steps were introduced in the sensing process in order to reach higher amplification of the impedimetric signal. After the sensing process outlined in Scheme 11A was finished, the interface was further stepwise reacted with biotinylated liposomes and avidin yielding a dendritic multilayer structure on the sensing surface [108], Scheme 11B. The electrode surface was significantly isolated by the liposomes, thus the interfacial electron transfer process was further perturbed and the R_{et} value was further increased. This allowed additional amplification of the sensing signal for the primary DNA hybridization process. The liposomes also decreased the non-specific adsorption of foreign proteins on the sensing interface. Even higher extent

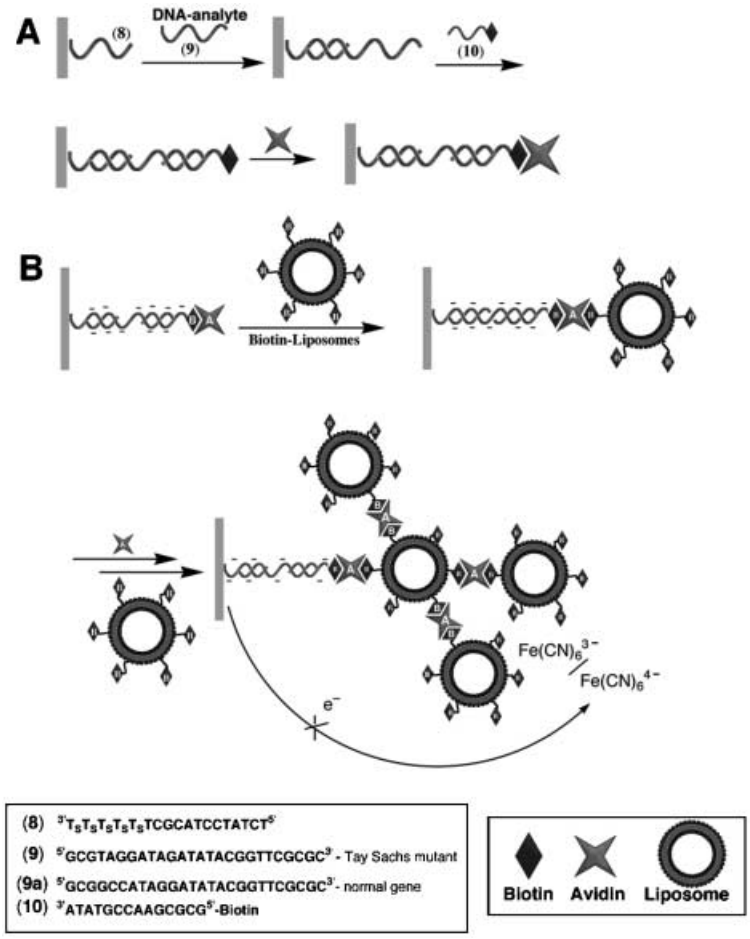

Scheme 11. Impedimetric DNA sensing amplified by the assembly of secondary superstructures: A) Primary DNA hybridization amplified by the secondary binding of a biotinylated-oligonucleotide and avidin. B) Primary DNA hybridization amplified by secondary binding of a biotinylated oligonucleotide followed by the formation of a multilayer dendritic superstructure composed of avidin units and biotinylated liposomes.

of the impedimetric signal amplification was reached when a biocatalytic process was used as amplification means. For this purpose, after the sensing interface was reacted with a biotinylated oligonucleotide according to the reaction sequence outlined in Scheme 11A, it was further reacted with avidin-HRP conjugates [118], Scheme 12A, or liposomes functionalized with avidin and HRP units [90], Scheme 12B. The HRP biocatalytic moieties were used to catalyze formation of the insoluble product (**7**) that precipitated on the sensing surface and resulted in the growing barrier for the interfacial electron transfer process. Thus, the sensing signal amplification was also controlled by the time-interval of the precipitation process.

A further route for the amplified detection of DNA by the biocatalyzed precipitation of an insoluble product on the electrode has involved the intercalation of doxorubicin (**11**) into a ds-DNA assembly at a Au electrode surface [119], Scheme 13. Doxorubicin intercalates only into double-stranded DNA, and thus its association with the electrode indicates the hybridization event between the sensing interface and the analyte DNA. The electrochemical reduction of the quinonoid intercalator stimulates electrocatalyzed O_2 reduction resulting in the generation of H_2O_2, which participates in the formation of the insoluble precipitant **7** in the presence of HRP and **6** in the solution. The impedimetric detection of the DNA hybridization event was amplified by the insulation of the electrode as a result of the precipitation process.

4.2. Impedimetric Sensing of Single-Base Mismatches in DNA Sequences

The specific detection of DNA mutants is a basic challenge in DNA analysis. Partial selectivity in DNA analysis was achieved by the application of a sensing interface that is capable to generate a single double-helix turn with the analyte DNA. The introduction of four-to-six mismatches between the sensing interface and the analyte DNA is sufficient to prevent hybridization and discriminate the mutants from fully complementary DNA [116]. A different approach to tailor specificity in DNA analysis involves the use of the different melting temperature of double-stranded DNA that includes variable numbers of base mismatches.

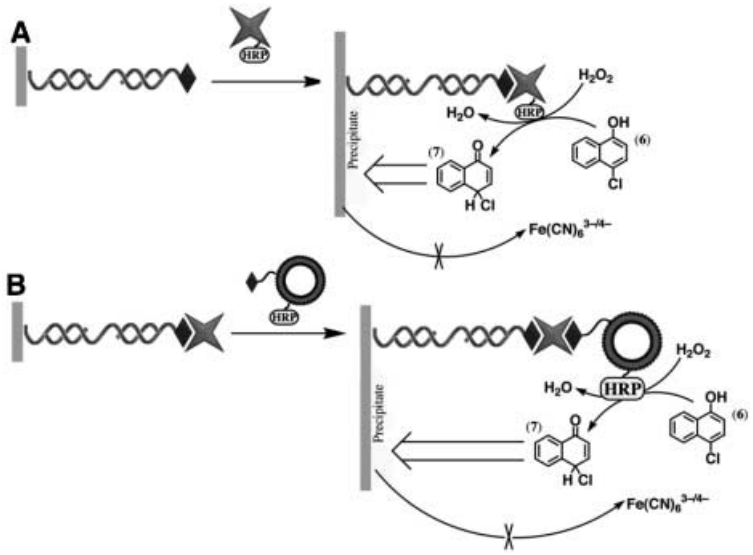

Scheme 12. Impedimetric DNA sensing amplified by biocatalytic reactions that follow the primary sensing events: A) Primary DNA hybridization amplified by the avidin-HRP biocatalyzed precipitation of the insoluble product on the electrode. B) Primary DNA hybridization amplified by the biocatalyzed precipitation of the insoluble product by an avidin/biotinylated-liposome-HRP superstructure.

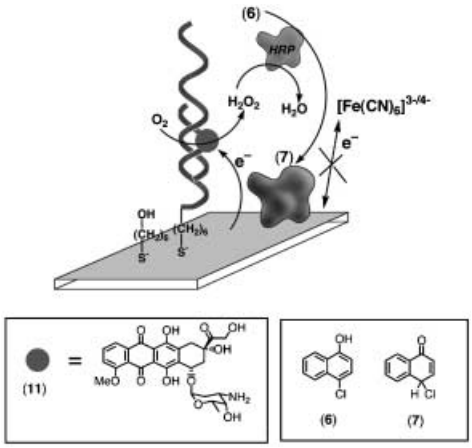

Scheme 13. Impedimetric DNA sensing amplified by precipitation of the insoluble product using electrochemical generation of H_2O_2 catalyzed by the redox active intercalator.

As the number of base mismatches increases, the melting temperature of the double-stranded DNA is lowered. This property has been used for the specific electrochemical analysis of DNA by controlling the hybridization temperature between the sensing nucleic acid and the analyzed DNA [125].

A method for the amplified detection of single base mismatches in DNA using Faradaic impedance spectroscopy as transduction means was developed [120]. The method is schematically presented in Scheme 14, where the detection of the 41-base mutant oligonucleotide (**12**), that includes a single mutation, the substitution of a guanine for an adenine in the normal sequence (**12a**), is illustrated. The thiolated oligonucleotide (**13**), which is complementary to the mutant or the normal gene **12** or **12a** up to the point of mutation, is assembled on a Au electrode and used as the active sensing interface. Interaction of the sensing interface with the mutant (**12**) or the oligonucleotide representing the normal sequence (**12a**) generates the respective double-stranded assembly on the electrode surface. The resulting interface is then reacted with the biotinylated base complementary to the mutation site in the mutant (e.g., biotinylated cytosine triphosphate, b-dCTP) in the presence of DNA polymerase I (Klenow fragment). In the presence of the double-stranded assembly that includes the mutant, the surface coupling of b-dCTP to the probe oligonucleotide proceeds. The resulting assembly is then interacted with an enzyme-linked avidin conjugate that catalyzes the precipitation of an insoluble product on the electrode surface. Specifically, avidin-alkaline phosphatase conjugate (avidin-AlkPh) was used, and its association with the sensing interface catalyzed the oxidative hydrolysis of 5-bromo-4-chloro-3-indoyl phosphate (**14**) to the insoluble indigo derivative (**15**). Precipitation of **15** occurs only if the single-base mutant hybridizes to the probe linked to the sensing surface. The biocatalyzed precipitation of **15** provides a means to amplify the detection process, and the extent of precipitate formed on the electrode surface is controlled by the amount of DNA mutant associated with the sensing interface, and the time-interval employed for the biocatalyzed precipitation of **15.** The insoluble product formed on the electrode alters the capacitance and electron transfer resistance at the conductive support. Figure 13A, curve a, shows the Faradaic impedance spectrum of the sensing interface modified with the probe oligonucleotide (**13**) using $[Fe(CN)_6]^{3-/4-}$ as redox label. Curve b shows the Faradaic impedance spectrum of the sensing interface after interaction with the mutant (**12**), 3×10^{-9} mol mL^{-1}, and curve c shows the spectrum after the sensing interface

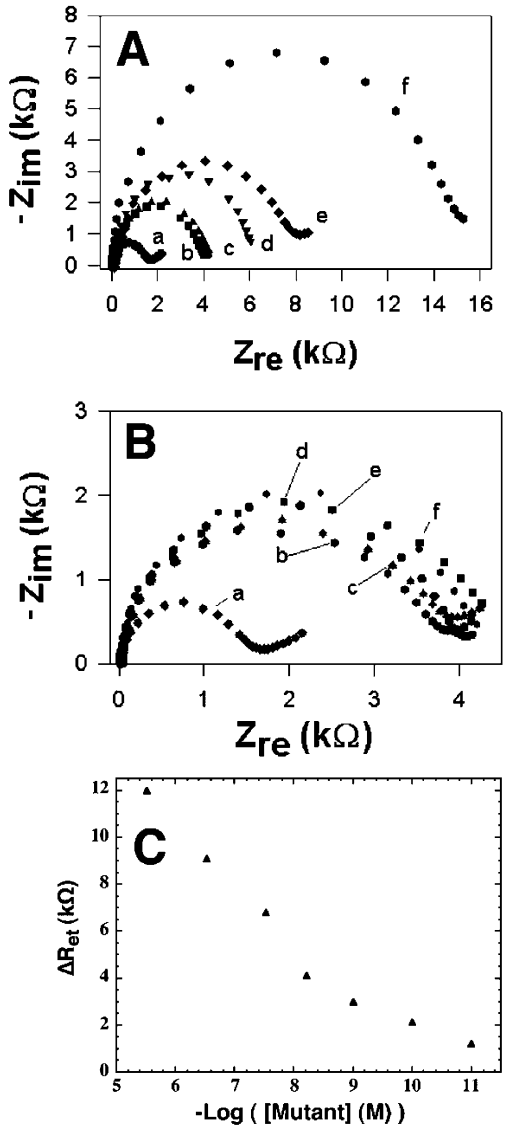

Fig. 13. Impedimetric sensing of DNA single-base mutation amplified by the precipitation of an insoluble product on the electrode: A) Faradaic impedance spectra corresponding to: a) The (**13**)-modified electrode. b) The (**13**)-modified electrode after interaction with the mutant DNA (**12**), 3×10^{-9} mol mL^{-1}. c) The ds-(**13**)/(**12**)-functionalized electrode after interaction with the biotinylated dCTP in the presence of Klenow fragment, 20 U · mL^{-1} in Tris-buffer, pH 7.8. d) After the interaction of the biotin-labeled ds-DNA-assembly with avidin-alkaline phosphatase conjugate, 100 nmol mL^{-1} in 0.1 M phosphate buffer solution for 15 minutes. e) After the precipitation of **15** biocatalyzed by alkaline phosphatase for 10 minutes, [**14**] $= 2 \times 10^{-1}$ M. f) After the precipitation of **15** biocatalyzed by alkaline phosphatase for 40 minutes. B) Faradaic impedance spectra corresponding to: a) The (**13**)-functionalized electrode. b) After the interaction of the (**13**)-functionalized electrode with the normal gene DNA (**12a**), 3×10^{-9} mol mL^{-1}. c–f) Repetition of the steps outlined in (A). C) Calbration plot corresponding to the changes in the electron transfer resistances of the electrode as a result of the precipitation of **15** upon the detection of different concentrations of **12.** (Reproduced from [120] with permission).

treatment with b-dCTP and polymerase. Curve d shows the spectrum of the resulting surface after treatment with avidin-AlkPh conjugate, and curves e–f show the spectra after the biocatalyzed precipitation of the insoluble product (**15**) was allowed to proceed for 10 minutes and 40 minutes, respectively. The electron transfer resistance increases from 1.6 kΩ to ca. 4.1 kΩ upon the formation of the double-stranded assembly between the probe (**13**) and the mutant (**12**) oligonucleotides. This is consistent with the electrostatic repulsion of the redox label from the electrode surface upon the formation of double-stranded assembly that introduces a barrier for the interfacial electron transfer. Although the treatment of the electrode with the polymerase and b-dCTP does not affect the interfacial electron transfer resistance, the association of the hydrophobic avidin-alkaline phosphatase conjugate introduces a barrier for the electron transfer, $R_{et} = 6.2$ kΩ. Biocatalyzed precipitation of **15** onto the electrode insulates the sensing surface and increases the electron transfer resistance to ca. 8.4 kΩ and ca. 16 kΩ after 10 and 40 minutes of precipitation, respectively. Thus, the primary sensing event was amplified by the binding of avidin-AlkPh conjugate and even further amplified by the biocatalyzed precipitation process. The Faradaic impedance spectra corresponding to the similar experiments performed with the oligonucleotide representing the normal sequence (**12a**) are shown in Figure 13B. It is evident that after the formation of the double-stranded assembly, $R_{et} = 3.9$ kΩ, no further increase in the electron transfer resistance is observed upon treatment of the surface with avidin-AlkPh conjugate and an attempt to precipitate the insoluble product (**15**). Thus, the successful analysis of **12** is attributed to the specific polymerase-mediated coupling of b-dCTP to the mutant assembly, resulting in further binding of the avidin-AlkPh conjugate and the biocatalyzed precipitation of **15.** A calibration plot for the analysis of the single-base mismatched DNA mutant was derived from the Faradaic impedance spectra obtained for different concentrations of the analyte, Figure 13C. The method was successfully applied for the analysis of DNA samples from blood for the Tay-Sachs genetic disorder. The method has enabled the detection of the mutants with the discrimination of homocygotic and heterocygotic carriers of the genetic disorder with no need for pre-PCR amplification.

Using a related approach single-base mismatches in DNA were identified applying negatively charged biotinylated liposomes as labels and Faradaic impedance spectroscopy as transduction means [108]. The method involves the coupling of the biotin-labeled base complementary to the mutation site as outlined in Scheme 14. The subsequent association of avidin and the biotin-labeled negatively charged liposomes yields an interface that blocks the interfacial electron transfer to the negatively charged redox probe $[Fe(CN)_6]^{3-/4-}$. The inhibition of the electron transfer process resulted in a high interfacial electron transfer resistance, R_{et}, which was monitored by Faradaic impedance spectroscopy.

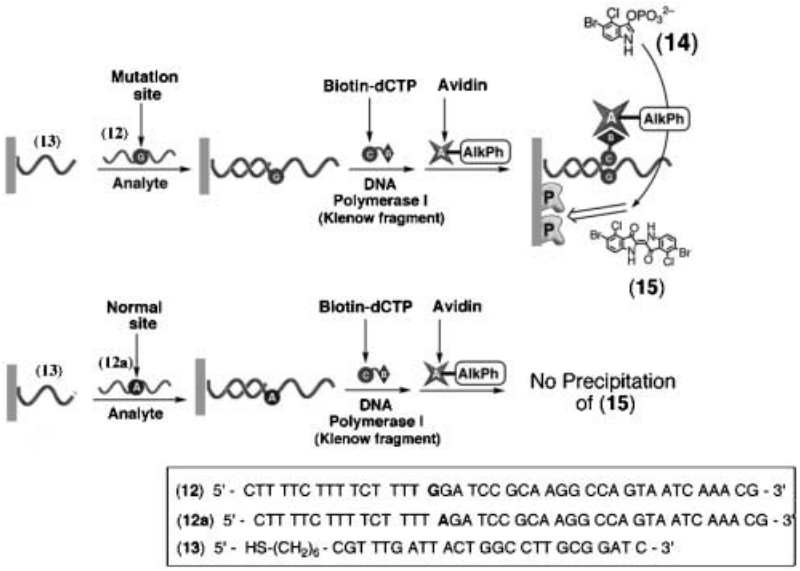

Scheme 14. Sensing of DNA single-base mutation amplified by precipitation of the insoluble product.

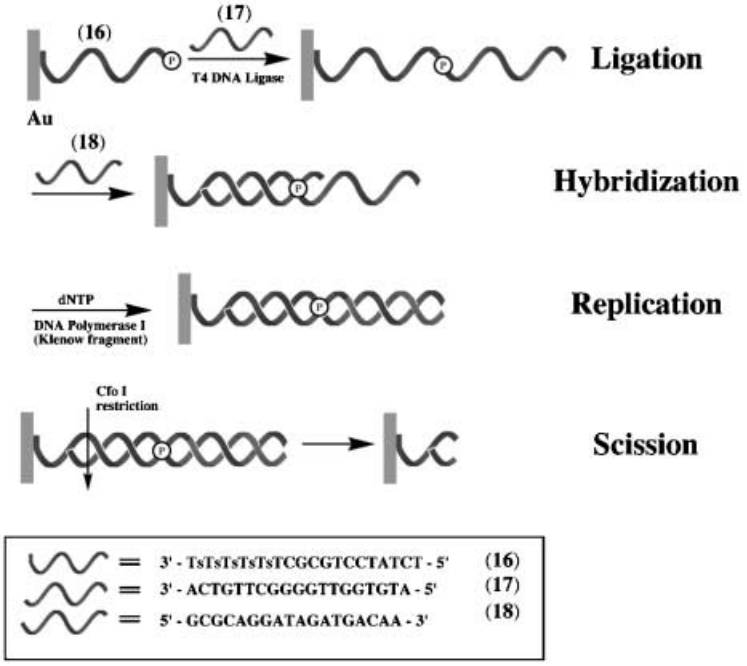

Scheme 15. Biocatalyzed ligation, replication and scission of single- and double-stranded DNA on electronic transducer (Ts = thymine thiophosphate).

4.3. Impedimetric Sensing of DNA and RNA Replication

The control of the interfacial properties of electrodes functionalized with nucleic acids has enabled the analysis of biocatalyzed transformations on surface confined nucleic acids by means of Faradaic impedance spectroscopy [122]. Enzyme induced ligation, replication and specific scission of DNA have been examined on electrode surfaces, Scheme 15. The thiolated 18-mer oligonucleotide primer (**16**) was assembled on a Au electrode and ligated to oligonucleotide (**17**) in the presence of ligase. The interfacial electron transfer resistance of the **16**-modified electrode, Figure 14, curve a, is $R_{et} = 0.44$ kΩ and it is increased upon ligation with **17** to $R_{et} = 1.33$ kΩ, curve b. This is consisted with the fact that negative charge was accumulated on the electrode upon ligation and the fact that $[Fe(CN)_6]^{3-/4-}$ was used as a redox probe. Hybridization of oligonucleotide (**18**) with the ligated product and the replication of the double-stranded assembly further increased the interfacial electron transfer resistance to $R_{et} = 1.9$ kΩ and 3.1 kΩ, respectively,

curves c – d, due to the accumulation of negative charges on the surface in the respective two processes. Treatment of the surface with the endonuclease CfoI that is specific to the double-stranded sequence 5′GCG/C3′ resulted in the decrease of the interfacial electron transfer resistance to R_{et} = 0.9 kΩ, Figure 14, curve e, due to the removal of nucleic acid residues upon the hydrolytic scission.

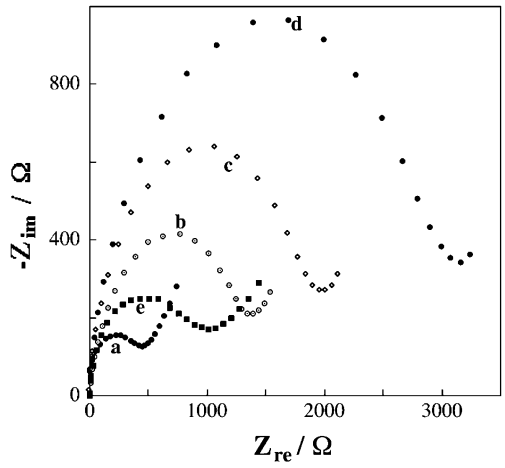

Fig. 14. Faradaic impedance spectra corresponding to the biocatalytic transformations of nucleic acid-functionalized electrode: a) **16**-functionalized electrode. b) After ligation of **17**, 3×10^{-5} M, with the **16**-functionalized electrode in the presence of ligase, 20 units, 37 °C, 30 minutes. c) After hybridization of the resulting assembly with **18**, 2.5×10^{-5} M, 2 h. d) After replication of the double-stranded assembly in the presence of dNTP, 1×10^{-3} M, and polymerase, 3 units, 37 °C, 30 minutes. e) After scission of the resulting assembly with endonuclease, CfoI, 10 units, 37 °C, 1 h. The impedance spectra were recorded within the frequency range 0.1 Hz – 50 kHz at the bias potential, 0.17 V; amplitude of alternating voltage, 5 mV, using $[Fe(CN)_6]^{3-/4-}$, 1×10^{-2} M, as the redox probe in 0.01 M phosphate buffer, pH 7.0.

An ultrasensitive detection of viral DNA was achieved with an amplified impedimetric sensing that does not need the PCR amplification process prior to the analysis. The method for analysis of the target viral DNA that involves the surface replication and concomitant labeling of the analyzed DNA is depicted in Scheme 16 [121]. The primer thiolated oligonucleotide (**19**), complementary to a segment of the target M13ϕmp8 DNA, was assembled on a Au electrode through a thiol functional group. The sensing interface was then treated with the analyte DNA of M13ϕmp8 (+)strand, and the resulting complex on the electrode surface was treated with a mixture of bases: dATP, dGTP, dTTP, dCTP, that included also biotinylated-dCTP (ratio $1:1:1:{}^{2}/_{3}:{}^{1}/_{3}$, nucleotides concentration of 1 mM) in the presence of DNA polymerase I, Klenow fragment (20 u mL^{-1}). Polymerization and the formation of a double-stranded assembly with the target DNA provides the first amplification step of the analysis of the viral DNA. Furthermore, the biotin tags into the replicated double-stranded assembly provide docking sites for the binding of the avidin-alkaline phosphatase conjugate. The associated enzyme biocatalyzed the precipitation of the insoluble material (**15**) on the electrode surface, thus providing the second amplification step for the analysis of the target DNA. The process was monitored by the Faradaic impedance spectroscopy. Figure 15, curve a, shows the impedance spectrum of the Au electrode functionalized with the primer oligonucleotide (**19**). The electron transfer resistance, R_{et}, increased upon the binding of the viral DNA from 3 kΩ to ca. 20 kΩ, curve b. This is consistent with the fact that binding of the high molecular weight DNA electrostatically repels the negatively charged redox label, $[Fe(CN)_6]^{3-/4-}$. The DNA polymerase-mediated

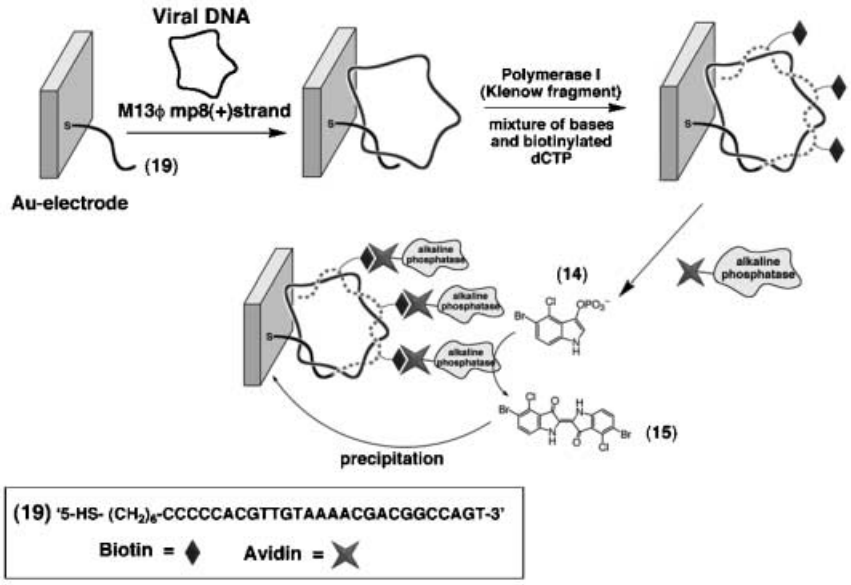

Scheme 16. Amplified impedimetric detection of viral DNA by the polymerase-induced replication of the analyte and the biocatalyzed precipitation of the insoluble product on the electrode (broken line shows replicated nucleic acid).

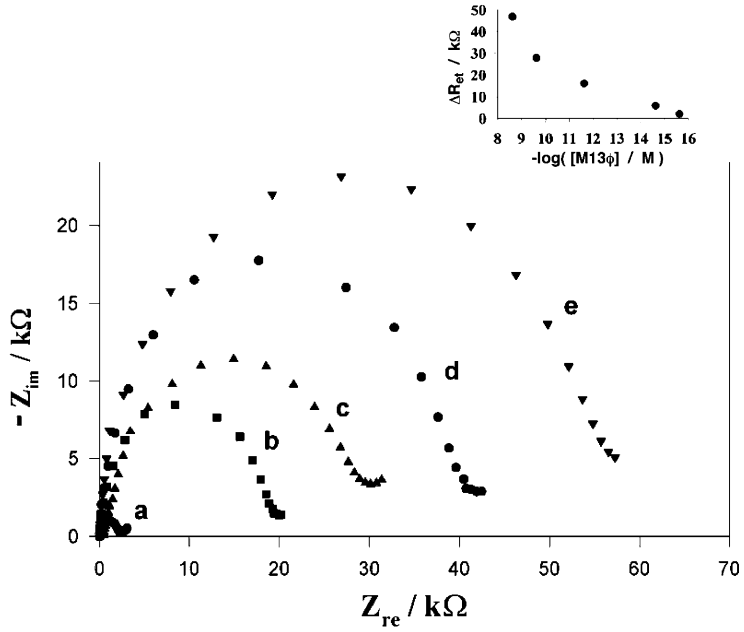

Fig. 15. Faradaic impedance spectra (Nyquist plots) of: a) The DNA probe (**16**)-functionalized electrode. b) After hybridization with the viral DNA, M13φmp8 (+)strand, 2.3×10^{-9} M. c) After the polymerase-induced replication and formation of the double-stranded assembly for 45 minutes. d) After the binding of the avidin-alkaline phosphatase conjugate to the surface. e) After the biocatalyzed precipitation of the insoluble product (**15**) for 20 minutes in the presence of **14**, 2×10^{-3} M. Inset: The changes in the electron transfer resistance, ΔR_{et}, upon the sensing of different concentrations of M13φ by the amplified biocatalyzed precipitation of **15** onto the electrode. The ΔR_{et} is the difference in R_{et} at the electrode after the precipitation of **15** for 20 min and R_{et} at the **16**-functionalized electrode. The impedance spectra were recorded within the frequency range 0.1 Hz – 50 kHz at the bias potential, 0.17 V; amplitude of alternating voltage, 10 mV, using $[Fe(CN)_6]^{3-/4-}$, 1×10^{-2} M, as the redox probe in 0.01 M phosphate buffer, pH 7.0. (Reproduced from [121] with permission).

synthesis of the complementary strand further increased the electron transfer resistance to $R_{et} = 33$ kΩ, due to the accumulation of the negative charges on the surface, curve c. Note that the polymerization does not double the R_{et} value, consistent with the partial replication of the complementary strand on the target DNA molecule. The binding of avidin-AlkPh conjugate, curve d, and the subsequent biocatalyzed precipitation of **15** onto the electrode surface, resulted in an insulating layer that introduced a high barrier for the interfacial electron transfer, $R_{et} = 58$ kΩ, curve e. A calibration plot was derived from the Faradaic impedance measurements with different concentrations of the viral DNA, Figure 15, inset. The amplification process involved in the impedimetric analysis of the target viral DNA allowed its detection with a sensitivity limit corresponding to 2×10^{-16} M. A similar approach was used for the amplified sensing of the 11 161-bases RNA of vesicular stomatitis virus (VSV) using reverse transcriptase as the replication biocatalyst [121]. The RNA detection limit was found to be 1×10^{-17} M (ca. 60 copies in 10 μL). These impedimetric methods for DNA and RNA analyses would find broad applicability in clinical diagnostics, environmental control, and food analysis.

5. Immunosensors and DNA-Sensors Based on Impedance Measurements on Semiconductive Devices

A semiconductor (e.g., doped Si) coated with a thin insulating layer (e.g., SiO_2) was used as a solid support for immunosensing with the impedimetric transduction of the recognition events [126 – 135]. Antigen or antibody units were immobilized at the Si/SiO_2-interface either by covalent coupling via silanization procedure or by incorporation into a polymeric membrane. Since the SiO_2 insulating layer yields an extremely high resistance, only capacitance values were derived from the impedance measurements [51, 136, 137]. For example, monoclonal antibodies were covalently linked to an aminosiloxane film associated with a Si/SiO_2 surface and the antigen α-fetoprotein could be detected with a sensitivity limit of 1 ng mL^{-1} (ca. 1.5×10^{-13} M) [138, 139]. A similar approach was used for detection of enterotoxin B where a capacitance decrease could be observed for 10 μg mL^{-1} (ca. 0.4×10^{-6} M) antigen concentration [140]. A flow-injection cell used with a capacitive sensor based on a semiconductor transducer allowed the impedance measurements of the antigen-antibody binding in real time [141]. In order to perform fast measurements in real time of the immuno-reaction, the capacitance was measured at a single frequency of 1 kHz. Simultaneous impedance spectra and

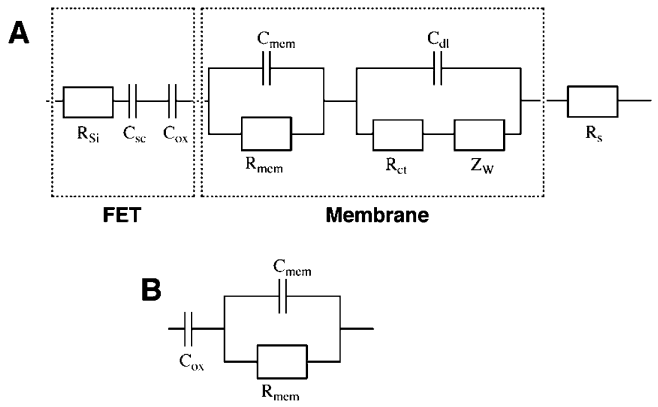

Scheme 17. A) Equivalent circuit of a FET device modified by a membrane film on the gate interface. B) Simplified equivalent circuit corresponding to a membrane-functionalized FET device.

FTIR-spectra measurements showed that interpenetration of the biospecies into the sensing membrane occurred, and the conformational change in state of the sensing membrane accompanied the binding of the antibodies to the sensing interface [142].

An important advantage of signal amplification is achieved by the integration of the semiconductor in the form of a field-effect transistor (FET) device [143]. Due to the complexity of impedance measurements on FET devices [144], some theoretical background will be discussed prior to the description of the results. The impedance of the membrane associated with the FET can be represented [145, 146] by the equivalent circuit shown in Scheme 17A. It consists of the input element of the FET device that is composed of the silicon-electrode resistance, R_{Si}, the space-charge capacitance, C_{sc}, and the oxide-insulator capacitance, C_{ox}, that is linked in series to the second element corresponding to the membrane, connected in series to the third element corresponding to the electrolyte solution resistance, R_s. The membrane element of the equivalent circuit is divided into two parts that are linked in series: One part includes the bulk membrane properties, i.e., the bulk capacitance of the membrane, C_{mem}, in parallel with the bulk membrane resistance, R_{mem}. The second part includes the interfacial properties of the membrane and is composed of the double-layer capacitance at the membrane interface, C_{dl}, in parallel with charge-transfer resistance at the membrane interface, R_{ct}, and the input of the Warburg impedance, Z_W, originating from the diffusion of ions to the membrane interface. This equivalent circuit can be simplified and depicted in the configuration shown in Scheme 17B. When the semiconductor operates in the inversion regime, C_{sc} is significantly smaller than C_{ox} and may be neglected. Also, the silicon-electrode resistance, and the solution resistance are substantially lower than the membrane resistance, R_{mem}. The interfacial features of the membrane have an important contribution to the circuit at low frequencies ($f \leq 5$ Hz) [147]. However, at high frequencies ($f \geq 5$ Hz), the interfacial properties of the membrane have no important contribution to the impedance features of the system, leading to the simple equivalent circuit where the C_{ox} unit is in series with an element consisting of the C_{mem} and R_{mem} in parallel, Scheme 17B. A relaxation time of the membrane, τ, can be experimentally deduced by the use of the electronic circuit that includes the FET/counter-electrode couple. The voltage applied between the counter-electrode and the source of the FET device, V_{GS}, leads to a source-drain current, I_D. The application of the small sinusoidal voltage variations on the counter-electrode, δV_{GS}, leads to small drain-current variations, δI_d. The transconductance, $g_m = \delta I_d / \delta V_{GS}$, is then frequency-dependent [148]. The output voltage, V_{out}, is related to I_D, g_m as given by Equation 10, where R represents electrical resistance in the measuring circuit.

$$V_{out} = -RI_d = -Rg_m V_{GS} \tag{10}$$

When a membrane is associated with the oxide gate layer, the applied potential V_{GS} is divided over the membrane and the oxide layers. Thus, the effective potential difference between the gate and source is smaller than the applied value V_{GS}. A frequency-dependent transfer function, $H(j\omega)$, defined by Equation 11, is introduced to relate to the applied voltage and to the output voltage, Equation 12.

$$H(j\omega) = \frac{1 + j\omega R_{mem} C_{mem}}{1 + j\omega R_{mem}(C_{mem} + C_{ox})} \tag{11}$$

$$V_{out} = Rg_m H(j\omega) V_{GS} \tag{12}$$

The frequency-dependent transfer function is defined by the elements of the simplified equivalent circuit, Scheme 17B. The theoretical dependence [145, 148] of the transfer function at variable frequencies is depicted in Figure 16. The method to extract the time constants τ_1, Equation 13, and τ_2, Equation 14, is shown in Figure 16.

$$\tau_1 = R_{mem}(C_{mem} + C_{ox}) \approx R_{mem} C_{ox} \tag{13}$$

$$\tau_2 = R_{mem} C_{mem} \tag{14}$$

The intersection of the two linear segments at low frequency yields the τ_1 value. Since at low frequencies the oxide layer capacitance is substantially higher than the adhered membrane, the term C_{mem} can be neglected, Equation 13. In contrast, at high frequencies, the impedance values of the membrane bulk resistance (R_{mem}) and the capacitance of the membrane (C_{mem}) tend to dominate the contribution from the oxide capacitance (C_{ox}), and therefore the latter can be neglected, Equation 14, [149]. The τ_2 value is extracted from the intersection of the two linear segments at high frequencies. By the determination of τ_2 and the value of R_{mem} from the independent C_{ox} measurement the membrane capacitance C_{mem} can be elucidated. The membrane capacitance is given by Equation 2, where δ is the film thickness (see Section 2).

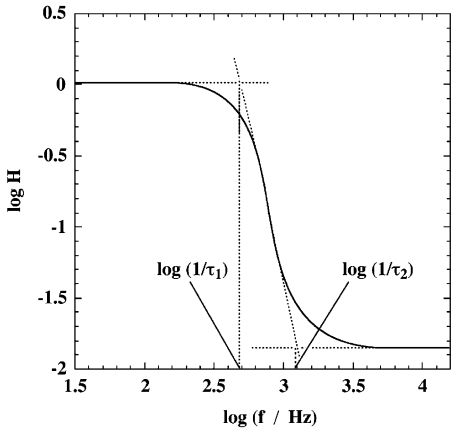

Fig. 16. Theoretical transfer function and extrapolation methods to extract the τ_1 and τ_2 values.

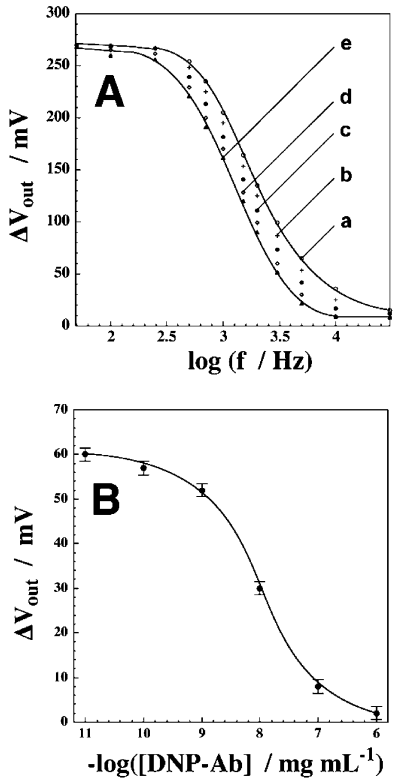

Fig. 17. Output voltages of the FET device at different frequencies corresponding to: a) The DNP-antigen-functionalized gate interface; and after its treatment with various concentrations of the DNP-antibody for 40 min: b) 1.6×10^{-9} mg mL^{-1}; c) 1.6×10^{-8} mg mL^{-1}; d) 1.6×10^{-7} mg mL^{-1}; e) 1.6×10^{-6} mg mL^{-1}. B) Calbration plot corresponding to the output voltage of the DNP-antigen-functionalized FET device for various concentrations of the DNP-Ab for a fixed time-interval of 40 minutes recorded at 30 kHz. (Reproduced from [150] with permission).

The ability to characterize, by the transconductance measurements, the thickness changes of protein layers associated to the aminosiloxane film linked to oxide layer of the gate interface, suggests that one may utilize the method for the transduction of biorecognition events that occur on the gate interface. Furthermore, as the method enables the determination of the average value of the thickness of the protein layer associated with the gate surface, and knowing independently the protein dimensions, one may estimate the surface coverage of the protein on the gate interface. Thus, impedance measurements on the FET device may provide a useful tool for the characterization of protein-functionalized FETs.

For example, DNP-antigen was covalently coupled to the siloxane layer atop of the gate interface of a FET [150]. The association of the DNP-Ab to the antigen layer was characterized by transconductance measurements as a means to analyze the antibody. Figure 17A, curve a, shows the output voltage, ΔV_{out} of the DNP-antigen-functionalized gate interface, while Figure 17A, curves b to e, show the output voltage, ΔV_{out} curves after the interaction of the antigen-functionalized FET device with different concentrations of the DNP-Ab in the range of $1.6 \times 10^{-9} - 1.6 \times 10^{-6}$ mg mL^{-1} for 40 min. The association of the DNP-Ab to the DNP-antigen interface results in a nonsymmetrical shift of the transconductance curve to low frequencies. Using Equations 14 and 2, the derived thickness of the DNP-Ab layer upon saturation corresponds to 40 ± 5 Å. The DNP-Ab exhibits a nonsymmetrical geometry with dimensions of ca. 50×70 Å. Realizing that the antibody has two-binding sites for the antigen and that the long Fc-axis of the antibody contributes mostly to the layer thickness, we expect that a random densely packed monolayer of the antibody would reveal an average thickness of ca. 42 Å, very close to the derived experimental value. Thus, the DNP-Ab/DNP-antigen complex creates a protein layer with a thickness that is almost identical to that expected for a random densely packed assembly. The sensing of variable concentrations of the DNP-Ab was performed by the interaction of the antigen-modified FET with the antibody for a fixed time interval that corresponds to 40 min [150]. Figure 17B shows the ΔV_{out} values observed upon the sensing of variable concentrations of the DNP-Ab. The ΔV_{out} values were extracted from the curves shown in Figure 17A at a frequency of 30 kHz, where the highest difference in the ΔV_{out} values is observed. It is evident that the antigen-functionalized FET device, and the respective electronic transduction method, enable to sense the DNP-Ab in the concentration range that corresponds to 0.1 ng mL^{-1} to 1 μg mL^{-1}. The linear response-range of the device is in the concentration range of 1 ng mL^{-1} to 100 ng mL^{-1} with a slope that corresponds to 22 mV dec^{-1}. The lower detection limit of the sensor for the analysis of the DNP-Ab is 0.6 ng mL^{-1}. The upper detection limit of the DNP-Ab by the FET sensor is 250 ng mL^{-1}, and at higher concentrations, the gate surface is saturated by the DNP-Ab. A similar approach was used to analyze cholera toxin using the impedance measurements on the FET device with the gate functionalized with the cholera toxin antibody [151]. The detection limit for analyzing cholera toxin was 1×10^{-11} M. Thus, the ability to characterize the structures of protein layers on the gate surface by FET devices by means of impedance spectroscopy provides a method to probe and

sense biorecognition events that occur on the gate surface of the FET devices [143, 150].

Similar impedance spectroscopy measurements were performed to characterize protein-functionalized gate surfaces of the FET devices, and specifically to structurally characterize enzyme-based biocatalytic interfaces associated with FETs [150]. For example, stepwise assembly of glucose oxidase multilayer structure on the gate interface of the FET device was followed by the impedance spectroscopy [150], Scheme 18. Figure 18 shows the transconductance at variable frequencies for the FET system that includes aminopropylsiloxane base film on the gate, curve a, and for the systems that include one to seven GOx layers, curves b – h. The assembly of the GOx layers on the aminosiloxane film results in a nonsymmetrical shift of the transconductance curve to lower frequencies. From the transconductance curves corresponding to the different numbers of GOx layers assembled on the gate surface, the thickness of the protein assembly consisting of variable layers was determined. Figure 18, inset, shows the changes in the protein film thickness upon the assembly of GOx layers. While the thickness of the first GOx layer is ca. 30 ± 5 Å, from the second layer the thickness increases almost linearly with an average thickness increment of ca. 45 ± 5 Å per layer. The slightly lower thickness of the first GOx layer may be attributed to the porous, rough, base aminosiloxane film. Taking into account that glucose oxidase has an average diameter of ca. 67 ± 5 Å, a densely packed monolayer of GOx is expected to exhibit a surface coverage of ca. 2.8×10^{-12} mol cm^{-2}. Since the experimental average thickness of GOx layers 2 to 7 is ca. 45 ± 5 Å that corresponds to ca. 65% of a densely packed monolayer, one could conclude that the surface coverage of GOx per layer is ca. 1.8×10^{-12} mol cm^{-2}. Thus, the thicknesses of the assemblies and coverages of each GOx-layer were derived from the

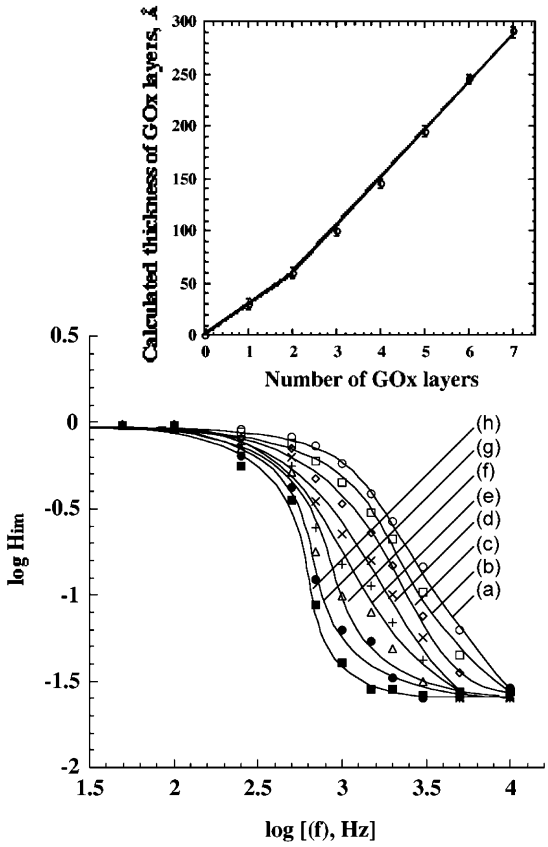

Fig. 18. Transconductance, H_{im}, curves at variable frequencies for: a) The aminopropylsiloxane-functionalized FET. b – h) After the deposition of one to seven layers of glucose oxidase, respectively. Inset: Thickness of protein layers as a function of number of deposited layers derived from the transconductance curves.

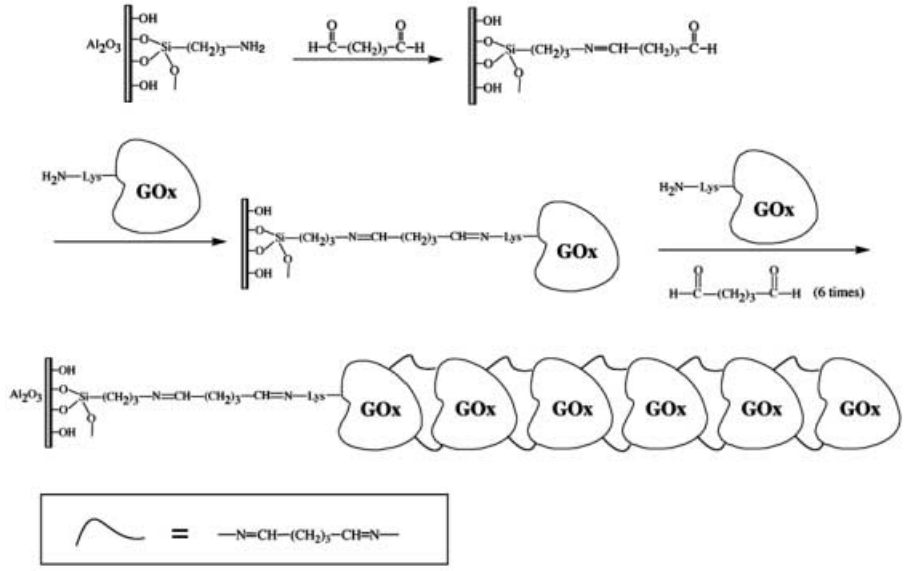

Scheme 18. Stepwise assembly of the glucose oxidase (GOx) multilayer structure on the gate interface of the FET device.

respective impedance spectra. The technique also allowed the quantitative characterization of enzyme structures associated as thin films with enzyme-functionalized FET devices (EnFETs) [26, 152].

The first successful attempts to achieve DNA-sensing using FET devices were made by measuring the imaginary part of the impedance at a fixed frequency as a function of the applied voltage. It has been shown that the immobilization of DNA on the gate surface results in a shift of the impedance function vs. the applied potential [153 – 156]. The shift is dependent on the amount of the immobilized DNA and it is enhanced upon hybridization of the complementary DNA [157]. However, the results have been demonstrated on very primitive systems including, for instance, hybridization of fully complementary poly(dA) and poly(dT) oligonucleotides and non-complementary poly(dA) and poly(dC) in a control experiment. Today, there are still insufficient experimental results on the DNA sensing on the basis of FET devices. However, the situation will probably improve in the near future and much effort will be directed towards new experiments with FET devices and the development of theoretical models, which can explain the experimental results. The FET-based DNA chips can be considered as a new tool for the simultaneous analysis of thousands of nucleic acids with a broad area of potential applications in biomedical research and clinical diagnostics, genomics, drug screening, environmental monitoring and food industry. They combine both the possibility of direct DNA hybridization detection without the use of labeled probes and the large integration ability of these active microelectronic devices (high density arrays of active areas up to 10^5 cm^{-2} can be achieved).

6. Application of Impedance Spectroscopy to Characterize Enzyme-Based Biosensors

Numerous kinds of enzyme-based biocatalytic electrodes were developed for their applications as amperometric biosensors, including layered and thin film enzyme assemblies [2, 3]. Monolayers of electrically contacted enzymes were produced by their covalent binding to functionalized thiolated self-assembled monolayers [158], by the reconstitution of apo-enzymes onto cofactor-functionalized monolayers [159, 160], or by the generation of integrated crosslinked $NAD(P)^+$-enzyme monolayers on electrode surfaces [14, 160]. Inter-protein electron transfer reactions were studied in layered protein-superstructures, including for example cytochrome c/cytochrome oxidase layered assembly [161]. Multilayers of enzymes were produced on electrode surfaces by the stepwise covalent binding [162] or by affinity interactions using, for instance, avidin-biotin binding units as crosslinking elements [7]. All of these protein structures have to be quantitatively characterized and their assembling should be followed prior to the electrochemical studies. These could be achieved by variety physical methods, including microgravimetric quartz-crystal microbalance measurements [21], surface plasmon resonance spectroscopy [163], ellipsometry measurements [164], and others. The fact that the association of proteins with electrodes generates a dielectric layer of insulating properties suggests that the impedance spectroscopy might provide a convenient and powerful tool to follow the interfacial build-up of the layered protein structures on electrodes.

Impedance spectroscopy was extensively used to follow changes of the interfacial properties of electrodes upon immobilization of enzymes and to characterize biocatalytic processes at enzyme modified electrodes. Blocking of the electrode surface with the bulky enzyme molecules [84, 165] and precipitation of insoluble materials due to the enzymatic reactions [84, 165, 166] were the main processes observed by Faradaic impedance spectroscopy. It has also been shown that the impedance spectroscopy could be used to characterize bioelectrocatalytic processes at enzyme-modified electrodes [160, 167].

6.1. Application of Impedance Spectroscopy to Characterize of Layered Enzyme Assemblies on Electrodes

Binding of protein/enzyme molecules to conductive supports results in the formation of a dielectric barrier for interfacial electron transfer processes. This allows measuring the extent of the electrode surface coverage with the protein units. For example, an aligned monolayer of covalently immobilized cytochrome c molecules was produced on a Au electrode surface and further reversible binding of cytochrome c oxidase to the cytochrome c-functionalized interface was studied by Faradaic impedance spectroscopy, Scheme 19, [34]. Figure 19A shows the Faradaic impedance spectrum of the cytochrome c-modified Au electrode, curve b, as well as the spectra in the presence of different concentrations of cytochrome oxidase, curves c – d. Cytochrome oxidase (COx) accepts electrons from the cytochrome c (Cyt c) in native electron transfer chains that lead to O_2 reduction to H_2O, and thus, it exhibits affinity binding to the cytochrome c molecules. As expected, the impedance spectra recorded in the presence of COx show the increase in the electron transfer resistance, R_{et}, at the electrode interface, originating from the association of the secondary COx layer onto the primary cytochrome c layer. This increase is controlled by the COx concentration in the solution, Figure 19B, consistent with the fact that COx binds reversibly to the cytochrome c monolayer to form the affinity complex COx/Cyt c on the electrode. The concentration-dependent changes of the interfacial electron transfer resistance has enabled one to derive the association constant of COx to the Cyt c monolayer, $K_a = 1.2 \times 10^7$ M^{-1}, using Benesi-Hildebrand method. Similarly, the association constants of the NAD^+-dependent enzymes (alcohol dehydrogenase or lactate dehydrogenase) to a NAD^+-monolayer functionalized Au electrode were determined by Faradaic impedance spectroscopy [34].

The Faradaic impedance spectroscopy was also applied to follow the kinetics of the reconstitution process of apo-

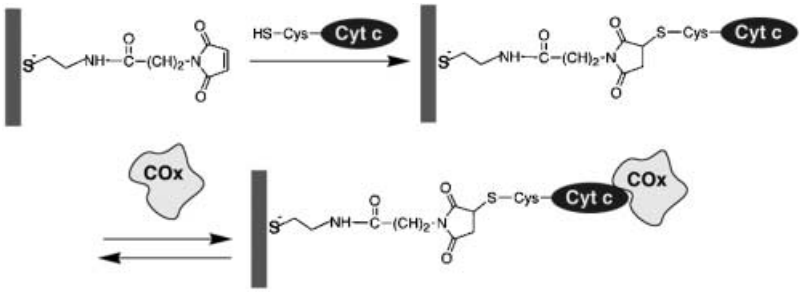

Scheme 19. Modification of a Au electrode with a cytochrome c monolayer and dynamic association of cytochrome oxidase (COx) to the modified electrode surface.

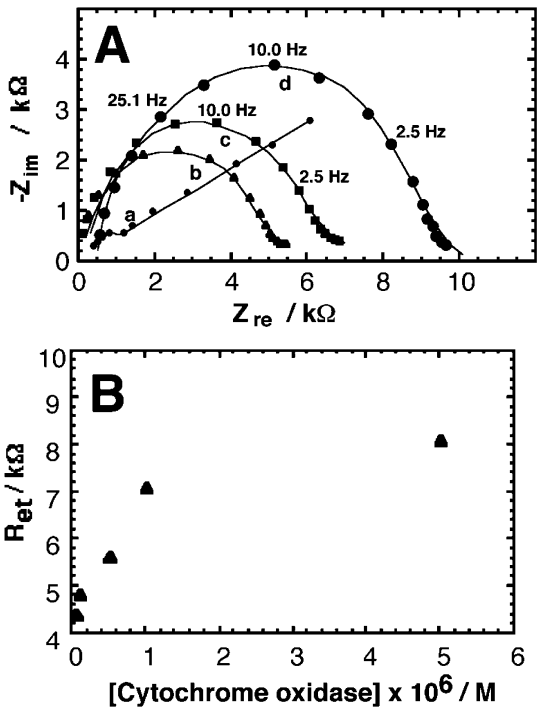

Fig. 19. Impedance measurements of the reversible binding of cytochrome oxidase (COx) to a cytochrome c-functionalized Au electrode. A) Nyquist diagrams (Z_{im} vs. Z_{re}) for the Faradaic impedance measurements performed at: a) A bare Au electrode. b) The cytochrome c monolayer-functionalized Au electrode. c, d) COx associated with the cytochrome c monolayer-functionalized electrode, [COx] = 0.5 μmol L^{-1} and 5.0 μmol L^{-1}, respectively. Numbers on the spectra show the frequency values for the selected points. The impedance spectra were recorded within the frequency range 0.1 Hz – 1.0 kHz at the bias potential, 0.17 V; amplitude of alternating voltage, 5 mV, using $[Fe(CN)_6]^{3-/4-}$, 1×10^{-2} M, as the redox probe in 0.01 M phosphate buffer, pH 7.0. B) Calibration plot corresponding to the interfacial electron transfer resistance, R_{et}, derived from the impedance spectra at different concentrations of COx. (Reproduced from [34] with permission).

glucose oxidase (apo-GOx) on an FAD-functionalized Au electrode [160]. A Au electrode was modified with a pyrroloquinoline quinone (PQQ, **20**) monolayer covalently bound to a self-assembled cystamine monolayer. Then an FAD-cofactor (**22**) was covalently bound to the PQQ monolayer using 3-aminophenylboronic acid (**21**) as a linker. Finally, the FAD-PQQ-functionalized Au electrode was reacted with apo-GOx to create the reconstituted glucose oxidase monolayer that exhibits electrical contact with the conductive support and reveals bioelectrocatalytic functions towards oxidation of glucose, Scheme 20. The reconstituted GOx catalyzed the oxidation of glucose, and the PQQ redox units provided the electron transport from the enzyme cofactor to the electrode. The Faradaic impedance spectra were recorded on the modified electrode after different time of the apo-GOx reconstitution process, Figure 20. As expected, the electron transfer resistance, R_{et}, was increased as the reconstitution time-interval was prolonged, leading to higher coverage of the electrode surface with the reconstituted GOx. The higher enzyme coverage resulted in a higher barrier for the interfacial electron transfer, thus producing the increased R_{et}. The increase of the R_{et} value with time reflects the kinetics of the apo-GOx binding to the functionalized electrode surface, Figure 20, inset. In parallel with the increased R_{et}, the increase of the biocatalytic functions of the reconstituted enzyme electrode towards the glucose oxidation was examined by cyclic voltammetry. The time-dependent increase in the amperometric responses of the electrode was overlapping with the time-dependent blocking of the electrode surface, thus indicating that both kinetics correspond to the same process of the enzyme reconstitution in the biocatalytically active form [160].

Similarly, the Faradaic impedance spectroscopy was applied to follow the build-up of various protein/enzyme monolayer and multilayer assemblies [84, 165].

6.2. Impedimetric Sensing of Electron Transfer Barriers Originating from Enzyme Biocatalytic Transformations at Electrodes

Biocatalytic reactions occurring at an electrode surface could yield the formation of an insoluble product that precipitates on the conductive support [84, 165, 166]. Alternatively the biocatalytic process could result in the degradation and dissolution of a polymer film or membrane associated with the electrode surface [168, 169]. The former process will result in the insulation of the conductive surface

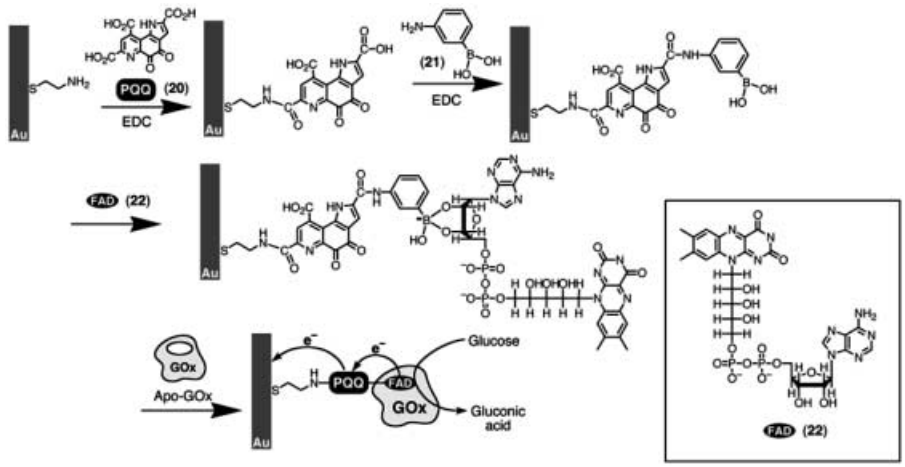

Scheme 20. Reconstitution of apo-glucose oxidase (apo-GOx) on a PQQ-phenylaminoboronic acid-FAD-functionalized Au electrode.

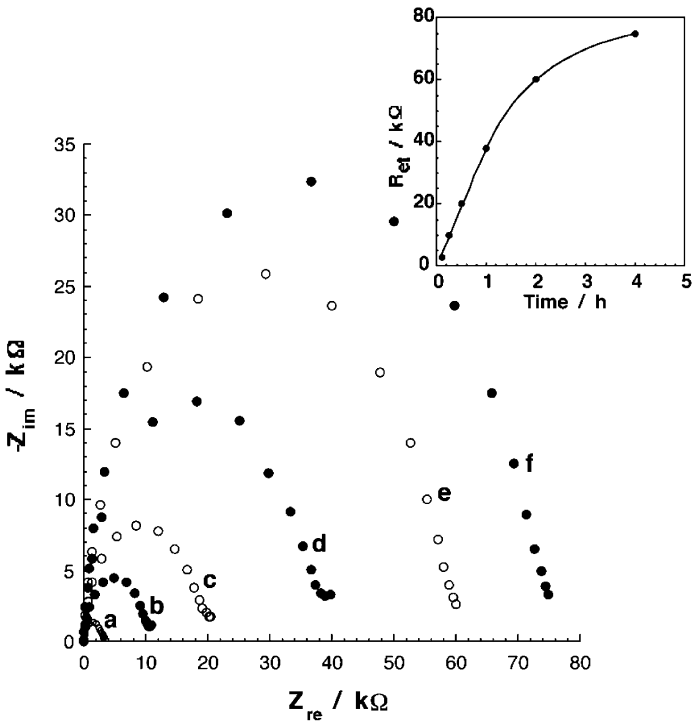

Fig. 20. Faradaic impedance spectra (Nyquist plots) of the PQQ-phenylaminoboronic acid-FAD-functionalized Au electrode at time-intervals of apo-GOx reconstitution, [apo-GOx] = 1 mg mL^{-1}: a) 0.1 h, b) 0.25 h, c) 0.5 h, d) 1 h, e) 2 h, f) 4 h. The data were recorded in 0.1 M phosphate buffer, pH 7.0, in the presence of $[Fe(CN)_6]^{3-/4-}$, 10 mM, biasing potential 0.17 V vs. SCE. The inset shows the R_{et} values of the electrode as the function of the reconstitution time. (Reproduced from [160] with permission).

and, thus, the electron transfer resistance will increase, whereas the latter process will result in the enhanced penetration of a redox probe through the membrane, and, therefore, the electron transfer resistance will decrease.

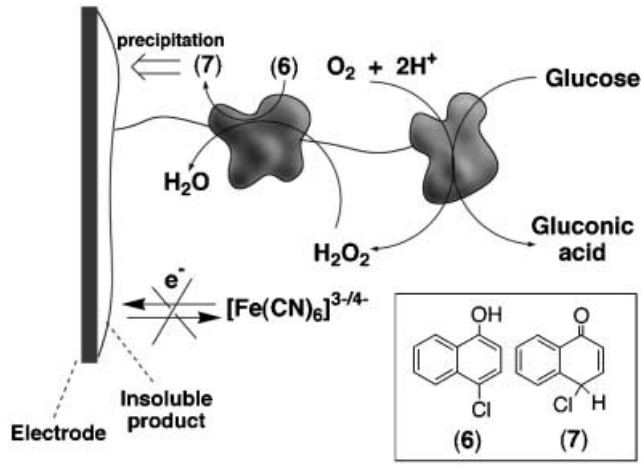

Scheme 21. Precipitation of the insoluble material (**7**) on the bi-enzyme-modified Au electrode as a result of glucose oxidation biocatalyzed by GOx monolayer.

Both processes were used to follow the biocatalytic reactions at electrode surfaces by impedance spectroscopy.

For example, a monolayer of horseradish peroxidase (HRP) assembled at a Au electrode surface catalyzed the biocatalytic oxidation of 4-chloro-1-naphthol (**6**) and formation of the insoluble product (**7**) in the presence of H_2O_2. This process was already discussed earlier as a method for labeling and amplifying of immunosensing and DNA-sensing events. However, it was also applied for the impedimetric analysis of H_2O_2 [166]. Since many oxidases (e.g., glucose oxidase, choline oxidase) generate H_2O_2 as a product of O_2 reduction upon enzymatic oxidation of the respective substrate, the HRP biocatalyzed formation of the insoluble film could be coupled with various enzymatic reactions. An integrated bi-enzyme system composed of a primary layer of HRP and a secondary layer of GOx was assembled on a Au electrode [166], Scheme 21. Addition of glucose to the O_2-containing solution resulted in the glucose

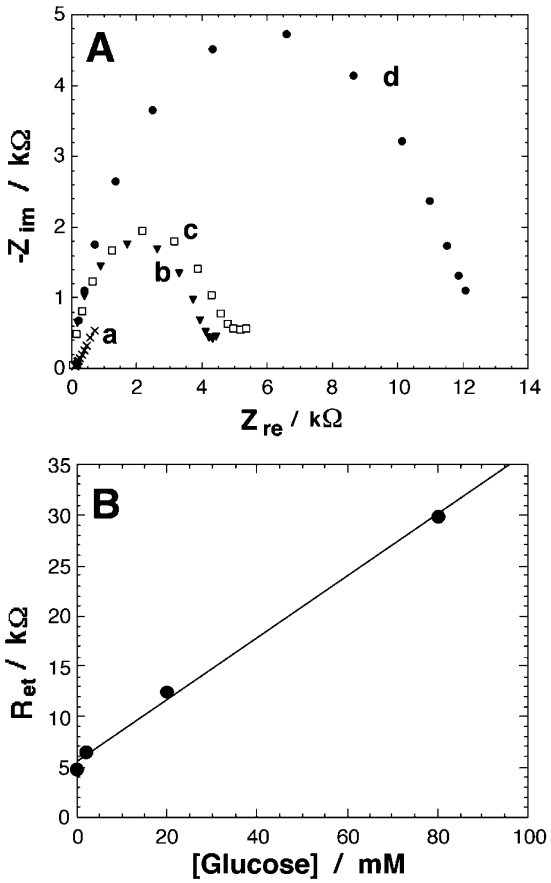

Fig. 21. Impedimetric analysis of glucose using the horseradish peroxidase-glucose oxidase (HRP-GOx)-modified electrode. A) Nyquist diagrams (Z_{im} vs. Z_{re}) for the Faradaic impedance measurements at: a) A bare Au electrode. b) HRP-monolayer modified Au electrode. c) Bi-enzyme (HRP-GOx)-modified Au electrode. d) HRP-GOx-modified Au electrode after incubation in the solution of **6**, 1 mM, and glucose, 2×10^{-2} M, for 10 minutes. The data were recorded in 0.1 M phosphate buffer, pH 7.0, in the presence of $[Fe(CN)_6]^{3-/4-}$, 10 mM, biasing potential 0.17 V vs. SCE. B) Calibration plot corresponding to the R_{et} values derived from the impedance spectra recorded for the HRP-GOx-modified electrode in the presence of different concentrations of glucose. The precipitation of **7** was performed for 10 minutes. (Reproduced from [166] with permission).

oxidation by the GOx layer and formation of H_2O_2 in the vicinity to the HRP layer. The HRP layer catalyzed the oxidation of **6** in the presence of H_2O_2 and formation of the **7** as an insoluble film on the electrode surface. The extent of the electrode surface insulation was probed by the Faradaic impedance spectroscopy in the presence of a redox probe, Figure 21A. The electron transfer resistance, R_{et}, was significantly higher as a result of the biocatalyzed precipitation of **7.** Since the amount of the in situ generated H_2O_2 is controlled by the GOx mediated oxidation of glucose, and as the content of the insoluble product **7** is controlled by the local concentration of H_2O_2, the R_{et} increase is dependent on the glucose concentration, Figure 21B. The thickness of the insoluble film on the electrode support is not only controlled by the concentration of glucose, but also affected by the time-interval used for the biocatalytic precipitation process. Thus, in order to derive the calibration plot shown in Figure 21B, the biocatalytic processes for different concentrations of glucose were probed by using a set of HRP-GOx bi-enzyme functionalized electrodes for a fixed time-interval. The extent of the electrode surface isolation and the amplification of the impedimetric signal originating from the biocatalytic process were dependent on how long the precipitation was allowed to proceed, thus, the longer time-intervals for the precipitation provided the higher sensitivity of the impedimetric analysis of glucose. A system of higher complexity composed of tri-enzyme layers (HRP, choline oxidase and choline esterase) was used for the similar impedimetric analysis of acetylcholine [165]. The primary reaction involved the acetylcholine esterase biocatalyzed hydrolysis of acetylcholine and formation of choline. The secondary reaction included the choline oxidase biocatalyzed oxidation of the in situ generated choline by oxygen and formation of H_2O_2. The latter product was than used for the HRP catalyzed precipitation of **7.** As before, the formation of the insoluble film on the electrode surface was probed by Faraday impedance spectroscopy allowing the amplified analysis of acetylcholine.

Alternatively, the enzymatic degradation of polymer films associated with electrodes was used to follow biocatalytic reactions by the impedance spectroscopy [168, 169]. For example, gelatin-coated electrodes were reacted with protease that resulted in the hydrolysis of the film and consequently led to the decrease of the interfacial electron transfer resistance at the electrode surface, thus allowing the impedimetric assay of the enzyme activity. Similar approach was used to monitor impedimetrically microbial activities (e.g., *Aspergillus versicolor*, *Cladosporium cladosporioides*, and *Chaetomium* species) by following the degradation of a polymer coating on the electrode surface [170].

6.3. Impedance Spectroscopy of Biocatalytic Reactions Involving Immobilized Enzymes

The primary scope of impedance spectroscopy is, however, the kinetic analysis of electrochemical reactions [38, 39], including those for redox-active biomolecules [171]. Thus, Faradaic impedance spectroscopy can be applied to study the kinetics of the electron transfer originating from bioelectrocatalytic reactions [160, 167]. This method is rarely used to characterize biosensors, although it might be a powerful method for examination of electrically contacted redox enzymes, and might provide complementary technique to direct current (DC) amperometric measurements. It should be noted, that for characterizing redox-active biomolecules by impedance spectroscopy no additional redox probe is added to the electrolyte solution, and the measured electron transfer process corresponds to the entire bioelectrocatalytic reaction provided by the biocatalyst. The impedance spectrum of a bioelectrocatalytically active enzyme-electrode allows the determination of the

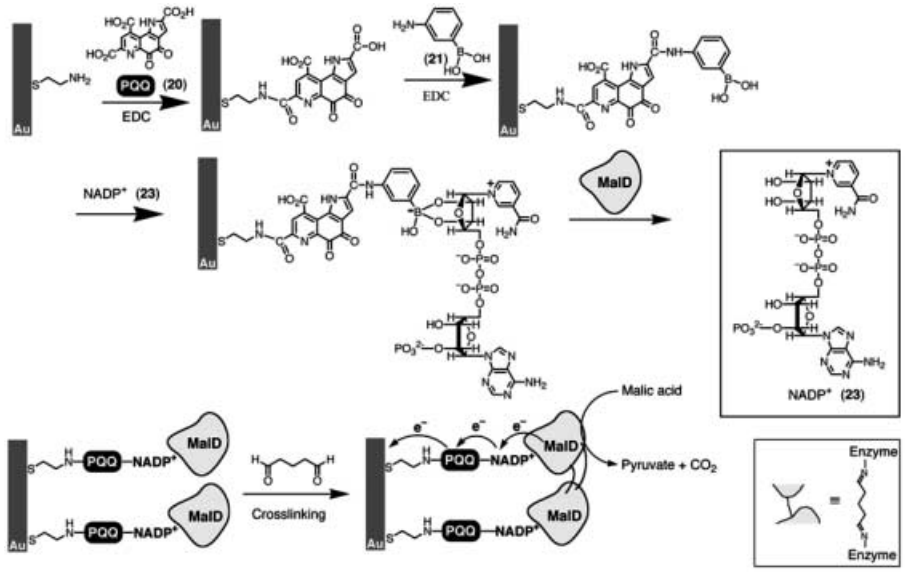

Scheme 22. Assembly of a crosslinked integrated malate dehydrogenase (MalD) biocatalytic electrode on a PQQ-phenylaminoboronic acid-$NADP^+$-functionalized surface.

electron transfer resistance, R_{et}, of the system. The electron transfer resistance translates into the exchange current under equilibrium, I_o, Equation 7, and then the respective heterogeneous electron transfer rate constant, k_{et}, can be derived, Equation 8 (see Section 2). Since enzyme-biosensors usually operate upon application of an overpotential, η, to provide the directional electron flow, the k_{et} dependence on the applied overpotential should be taken into account, Equation 15, where $\alpha \approx 0.5$ is the electron transfer coefficient, η is the overpotential applied to the biocatalytic electrode upon the impedance measurements, and all other parameters are the same as in Equations 7 and 8.

$$I_o = n F A k_{et}[S] \exp[\frac{(-\alpha n F \eta)}{RT}] \quad (15)$$

It should be noted, that the overpotential, η, is determined in respect to the standard potential, E°, of the electron transfer mediator providing the electron transport between the redox enzyme and the electrode support. Since the exchange current, I_o, is controlled by the substrate concentration (under condition that the enzyme is not saturated by the substrate), the electron transfer resistance of the electrode is also controlled by the substrate concentration. Thus, the substrate concentration can be analyzed by the impedance spectroscopy following R_{et} values and k_{et} corresponding to the limiting step in the bioelectrocatalytic oxidation (or reduction) of the substrate can be derived.

Bioelectrocatalytic performance of an integrated electrode composed of a self-assembled pyrroloquinoline quinone (PQQ, **20**) mediator monolayer, covalently bound $NADP^+$-cofactor (**23**), and associated with the cofactor and crosslinked malate dehydrogenase (MalD) enzyme was studied by the impedance spectroscopy [160], Scheme 22. Figure 22A shows the Faradaic impedance spectra of the biocatalytic electrode in the presence of different concentrations of the substrate malic acid. While the spectrum measured in the absence of malic acid, curve a, shows a very large electron transfer resistance, $R_{et} > 1$ MΩ, the values of the electron transfer resistance decrease upon increasing the malic acid concentration, curves b – h, reaching $R_{et} = 10$ kΩ at 8 mM of malic acid (note the different scales in the main graph and the inset). Figure 22B shows the calibration plot of R_{et} at various concentrations of malic acid. Using Equations 7 and 15, and taking into account that the spectra were recorded at $E = 0.25$ V (vs. SCE) ($\eta = 0.38$ V vs. the potential of the terminal electron mediator PQQ, $E^\circ = -0.13$ V [172]), the electrochemical rate constant can be expressed by the following equation: $k_{et} \approx 2.56 \times 10^{-3} ([S]R_{et})^{-1}$, where [S] is malic acid concentration (mol m^{-3}). It has been found that $[S]R_{et}$ has a constant value of ca. 6.8×10^4 mol m^{-3} Ω and that the electrochemical rate constant is equal to $k_{et} \approx 3.8 \times 10^{-6}$ cm s^{-1} [160]. Taking into account the surface coverage of MalD, $\Gamma_{MalD} = 1.15 \times 10^{-12}$ mol cm^{-2}, found by microbalance measurements, the overall rate constant that reflects the reaction of malic acid with the biocatalytic enzyme assembly was calculated, $k_{overall} = 8 \times 10^5$ M^{-1} s^{-1}.

7. Conclusions and Perspectives

This review has addressed recent advances in the applications of impedance spectroscopy to characterize the structure and functional operation of various kinds of biosensors, including immunosensors, DNA sensors and biocatalytic enzyme-based biosensors. Specifically, the use of impedance spectroscopy to follow the build-up of the biological structures on conductive supports (e.g., monolayers and

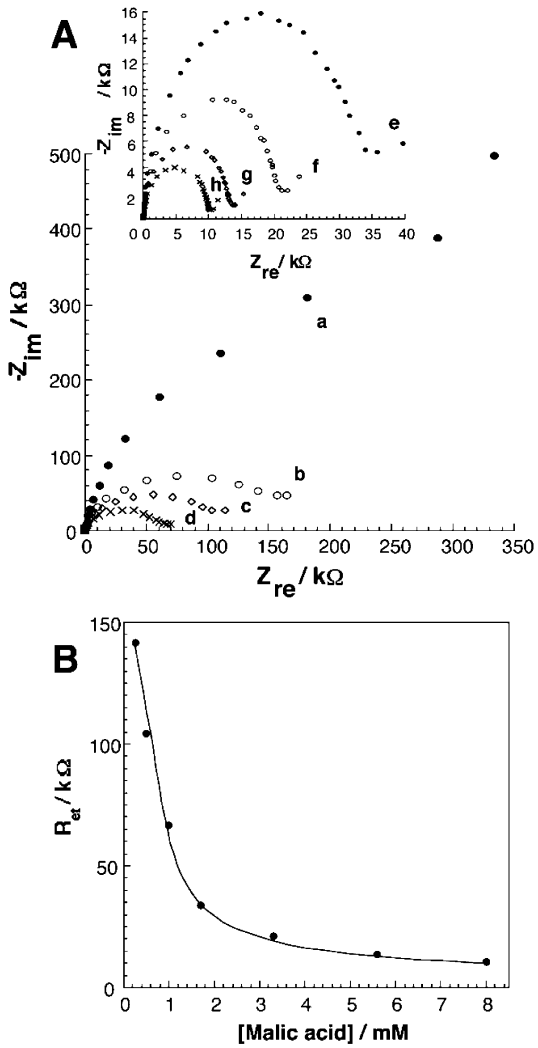

Fig. 22. Faradaic impedance spectra (Nyquist plots) of the integrated biocatalytic electrode obtained by crosslinking of malate dehydrogenase (MalD) associated with the PQQ-phenylaminoboronic acid-$NADP^+$-functionalized Au electrode in the presence of different concentrations of malic acid: a) 0 mM, b) 0.25 mM, c) 0.5 mM, d) 1.0 mM, e) 1.7 mM, f) 3.3 mM, g) 5.6 mM, h) 8.0 mM. Note the different scales in the main part of the graph and in the inset. The data were recorded in 0.1 M Tris-buffer, pH 7.0, with 10 mM $CaCl_2$, under Ar, biasing potential 0.25 V. B) Calibration plot corresponding to the electron transfer resistance, R_{et}, of the system at different concentrations of malic acid. (Reproduced from [160]) with permission).

multilayers of protein/enzyme units), to observe the affinity interactions of biomolecules (such as antigen-antibody binding, oligonucleotide hybridization on electrodes), to monitor biocatalytic reactions (e.g., DNA replication, ligation or enzymatic reactions resulting in the formation of insoluble products) were discussed. Different kinds of the impedance spectroscopy (including non-Faradaic capacitance measurements, Faradaic impedance spectroscopy in the presence of an external redox probe, transconductance measurements with field-effect transistors) were utilized in the different biosensor systems. The theoretical background of the different methods and their practical applications in analytical procedures were outlined in the article. The use of impedance spectroscopy as an electronic readout signal of novel biosensor protocols, such as the detection of a single-base mutations in DNA, or the amplified detection of viral DNA via replication were demonstrated. Furthermore, impedance spectroscopy offers a very sensitive method to follow time-dependent protein binding to electrodes, e.g., the reversible association/dissociation of antigen-antibody complexes on electrodes or the reconstitution of apo-enzymes on cofactor-functionalized electrodes. Combination of the impedance spectroscopy with other physical methods (such as surface plasmon resonance, ellipsometry, quartz-crystal microbalance, FTIR-spectroscopy, photoelectrochemistry) is especially productive to characterize the interfacial properties of sensing and bioelectronic devices.

Faradaic impedance spectroscopy is a time-consuming analysis method. The need to record the impedance features within a broad region of frequencies requires a typical duration time for an impedance spectrum experiment of 15 – 20 minutes. Despite this limitation, impedance spectroscopy provides a valuable tool to characterize basic features of the electrode interface, and to follow quantitatively chemical/biochemical events occurring on the electrode support (electron transfer resistances, interfacial electron transfer rate constants, interfacial capacitances). A possible path to circumvent the long-time interval for analyzing the substrate by impedance spectroscopy may be, however, the use of a single frequency value (or limited frequency range) for analysis. This method may introduce, however, less accurate results.

Broad applications of impedance measurements in different areas (e.g., clinical analyses, food processing, environmental control, etc.) can be easily envisaged. For instance, impedance measurements have already found practical use in the rapid analysis of meat quality [173], or the detection of food pathogenic bacteria [174, 175]. Impedance methods were successfully applied to electrodes modified with whole biological cells, and their growth and changes upon influence of external factors were electronically transduced by means of impedance measurements [176 – 178]. For example, the electrical properties of human umbilical vein endothelial cell monolayers on electrode surfaces have been studied by impedance spectroscopy in real time [177]. These measurements allowed the direct observation of the effect of inflammatory agents such as cytochalasin in real time. There are on-going studies directed to the impedimetric monitoring of bacteria growth [179], motility, spreading and mortality of insect cells [180], and drug screening using cells associated with electrode surfaces [181]. The whole-cell analysis could be performed impedimetrically on miniaturized chips that allows fast multi-channel cell screening [182]. *In vivo* impedance measurements on nerves and surrounding skeletal muscles in rats and human body could find important applications in biology and medicine [183]. Electrical impedance endotomography was developed for medical applications, for example for prostate

imaging [184]. Impedance spectroscopy certainly gained its recognition as a versatile electronic readout signal of biosensing events on conductive or semiconductive supports. The continuous progress in the development of new specific sensing interfaces such as imprinted polymers [185] or insect receptors [186] suggests that impedance spectroscopy could provide an electronic transduction means for these new analytical devices. Multi-channel semiconductive arrays associated with field-effect transistors and functionalized with DNA molecules could employ impedance measurements as a platform for rapid gene analysis.

8. Acknowledgement

The support of our research activities in the area of bioelectronics by the Israel Ministry of Science, the European Community (ATOMS project) and the German-Israeli Program (DIP) is acknowledged.

9. References

[1] I. Willner, *Science* **2002**, *298*, 2407.
[2] I. Willner, E. Katz, *Angew. Chem. Int. Ed.* **2000**, *39*, 1180.
[3] I. Willner, E. Katz, B. Willner, in *Biosensors and Their Applications* (Eds: V. C. Yang, T. T. Ngo), Kluwer Academic Publishers, New York **2000**, ch. 4, pp. 47.
[4] A. Heller, *Acc. Chem. Res.* **1990**, *23*, 128.
[5] W. Göpel, P. Heiduschka, *Biosens. Bioelectron.* **1995**, *10*, 853.
[6] C.-J. Zhong, M. D. Porter, *Anal. Chem.* **1995**, *67*, 709A.
[7] C. Bourdillon, C. Demaille, J. Gueris, J. Moiroux, J.-M. Savéant, *J. Am. Chem. Soc.* **1993**, *115*, 12264.
[8] C. Bourdillon, C. Demaille, J. Moiroux, J.-M. Savéant, *J. Am. Chem. Soc.* **1994**, *116*, 10328.
[9] C. Bourdillon, C. Demaille, J. Moiroux, J.-M. Savéant, *Acc. Chem. Res.* **1996**, *29*, 529.
[10] K. R. Rogers, *Mol. Biotechnol.* **2000**, *14*, 109.
[11] M. Yang, M. E. McGovern, M. Thompson, *Anal. Chim. Acta* **1997**, *346*, 259.
[12] I. Willner, E. Katz, B. Willner, in *Electroanalytical Methods of Biological Materials* (Eds: A. Brajter-Toth, J. Q. Chambers), Marcel Dekker, New York **2002**, pp. 43.
[13] C. N. Campbell, D. Gal, N. Cristler, C. Banditrat, A. Heller, *Anal. Chem.* **2002**, *74*, 158.
[14] A. Bardea, E. Katz, A. F. Bückmann, I. Willner, *J. Am. Chem. Soc.* **1997**, *119*, 9114.
[15] J. Anzai, H. Takeshita, Y. Kobayashi, T. Osa, T. Hoshi, *Anal. Chem.* **1998**, *70*, 811.
[16] I. Willner, S. Rubin, Y. Cohen, *J. Am. Chem. Soc.* **1993**, *115*, 4937.
[17] R. S. Sethi, *Biosens. Bioelectron.* **1994**, *9*, 243.
[18] P. N. Bartlett, P. Tebbutt, R. C. Whitaker, *Prog. React. Kinet.* **1991**, *16*, 55.
[19] R. M. Ianniello, T. J. Lindsay, A. M. Yacynych, *Anal. Chem.* **1982**, *54*, 1980.
[20] A. L. Ghindilis, I. N. Kurochkin, *Biosens. Bioelectron.* **1994**, *9*, 353.
[21] M. Lion-Dagan, I. Ben-Dov, I. Willner, *Colloids Surf. B* **1997**, *8*, 251.
[22] I. Ben-Dov, I. Willner, E. Zisman, *Anal. Chem.* **1997**, *69*, 3506.
[23] A. Bardea, A. Dagan, I. Ben-Dov, B. Amit, I. Willner, *Chem. Commun.* **1998**, 839.
[24] C. K. O'Sullivan, R. Vaughan, G. G. Guilbault, *Anal. Lett.* **1999**, *32*, 2353.
[25] N. Kazanskaya, A. Kukhtin, M. Manenkova, A. N. Reshetilov, L. Yarysheva, O. Arzhakova, A. Volynskii, N. Bakeyev, *Biosens. Bioelectron.* **1996**, *11*, 253.
[26] M. Zayats, A. B. Kharitonov, E. Katz, A. F. Bückmann, I. Willner *Biosens. Bioelectron.* **2000**, *15*, 671.
[27] V. Pardo-Yissar, E. Katz, J. Wasserman, I. Willner, *J. Am. Chem. Soc.* **2003**, *125*, 622.
[28] S. M. Amador, J. M. Pachence, R. Fischetti, J. P. McCauley, Jr., A. B. Smith, J. K. Blasic, *Langmuir* **1993**, *9*, 812.
[29] D. Hobara, K. Niki, C. Zhou, G. Chumanov, T. M. Cotton, *Colloids Surf. A* **1994**, *93*, 241.
[30] B. Liedberg, C. Nylander, I. Lundström, *Biosens. Bioelectron.* **1995**, *10*, i.
[31] C. E. Jordan, R. M. Corn, *Anal. Chem.* **1997**, *69*, 1449.
[32] O. A. Raitman, E. Katz, A. F. Bückmann, I. Willner, *J. Am. Chem. Soc.* **2002**, *124*, 6487.
[33] O. A. Raitman, F. Patolsky, E. Katz, I. Willner, *Chem. Commun.* **2002**, 1936.
[34] A. B. Kharitonov, L. Alfonta, E. Katz, I. Willner, *J. Electroanal. Chem.* **2000**, *487*, 133.
[35] D. Athey, M. Ball, C. J. McNeil, R. D. Armstrong, *Electroanalysis* **1995**, *7*, 270.
[36] T. M. Nahir, E. F. Bowden, *J. Electroanal. Chem.* **1996**, *410*, 9.
[37] H. S. Bresler, M. J. Lenkevich, J. F. Murdock, Jr., A. L. Newman, R. O. Robbin, in *Biosensor Design and Application*, ACS Symp. Ser. **1992**, *511*, 89.
[38] A. J. Bard, L. R. Faulkner, *Electrochemical Methods: Fundamentals and Applications*, Wiley, New York, **1980.**
[39] Z. B. Stoynov, B. M. Grafov, B. S. Savova-Stoynova, V. V. Elkin, *Electrochemical Impedance*, Nauka, Moscow, **1991.**
[40] J. E. B. Randles, *Discuss Faraday Soc.* **1947**, *1*, 11.
[41] B. V. Ershler, *Discuss Faraday Soc.* **1947**, *1*, 269.
[42] G. Y. Champagne, D. Belanger, G. Fortier, *Bioelectrochem. Bioenerg.* **1989**, *22*, 159.
[43] D. Savitri, C. K. Mitra, *Bioelectrochem. Bioenerg.* **1999**, *48*, 163.
[44] A. Bardea, E. Katz, I. Willner, *Electroanalysis* **2000**, *12*, 1097.
[45] J. Janata, *Critical Rev. Anal. Chem.* **2002**, *32*, 109.
[46] M. Pravda, M. P. Kreuzer, G. G. Guilbault, *Anal. Lett*. **2002**, *35*, 1.
[47] K. E. Sapsford, P. T. Charles, C. H. Patterson, F. S. Ligler, *Anal. Chem.* **2002**, *74*, 1061.
[48] P. B. Luppa, L. J. Sokoll, D. W. Chan, *Clin. Chim. Acta* **2001**, *314*, 1.
[49] W. M. Mullett, E. P. C. Lai, J. M. Yeung, *Methods* **2000**, *22*, 77.
[50] T. L. Fare, M. D. Cabelli, S. M. Dallas, D. P. Herzog, *Biosens. Bioelectron.* **1998**, *13*, 459.
[51] C. Berggren, B. Bjarnanson, G. Johansson, *Electroanalysis* **2001**, *13*, 173.
[52] W. Laureyn, D. Nelis, P. Van Gerwen, K. Baert, L. Hermans, R. Magnée, J.-J. Pireaux, G. Maes, *Sens. Actuat. B* **2000**, *68*, 360.
[53] P. Van Gerwen, W. Laureyn, W. Laureys, G. Huyberechts, M. O. De Beeck, K. Baert, J. Suls, W. Sansen, P. Jacobs, L. Hermans, R. Mertens, *Sens. Actuat. B* **1998**, *49*, 73.
[54] J. J. Valdes, J. G. Wall, J. James, P. Chambers, M. E. Eldefrawi, *Johns Hopkins APL Technical Digest* **1988**, *9*, 4.
[55] M. E. Eldefrawi, S. M. Sherby, A. G. Andreou, N. A. Mansour, Z. Annau, N. A. Blum, J. J. Valdes, *Anal. Lett.* **1988**, *21*, 1665.

[56] S. C. Pak, W. Penrose, P. J. Hesketh, *Biosens. Bioelectron.* **2001**, *16*, 371.
[57] R. F. Taylor, I. G. Marenchic, R. H. Spencer, *Anal. Chim. Acta* **1991**, *249*, 67.
[58] H. S. Bresler, M. J. Lenkevich, J. F. Murdock, A. L. Newman, R. O. Robin, *ACS Symp. Ser.* **1992**, *511*, 89.
[59] T. A. Sergeyeva, N. V. Lavrik, S. A. Piletsky, A. E. Rachkov, A. V. El'skaya, *Sens. Actuat. B* **1996**, *34*, 283.
[60] T. A. Sergeyeva, N. V. Lavrik, A. E. Rachkov, Z. I. Kazantseva, A. V. El'skaya, *Biosens. Bioelectron.* **1998**, *13*, 359.
[61] M. S. DeSilva, Y. Zhang, P. J. Hesketh, G. J. Maclay, S. M. Gendel, J. R. Stetter, *Biosens. Bioelectron.* **1995**, *10*, 675.
[62] S. Hardeman, T. Nelson, D. Beirne, M. DeSilva, P. J. Hesketh, G. J. Maclay, S. M. Gendel, *Sens. Actuat. B* **1995**, *24–25*, 98.
[63] O. A. Sadik, H. Xu, E. Gheorghiu, D. Andreescu, C. Balut, M. Gheorghiu, D. Bratu, *Anal. Chem.* **2002**, *74*, 3142.
[64] H. O. Finklea, in: *Electroanalytical Chemistry*, A. J. Bard, I. Rubinstein (Eds.), Marcel Dekker, New York, 1996, Vol. 19, pp. 109.
[65] M. Knichel, P. Heiduschka, W. Beck, G. Jung, W. Göpel, *Sens. Actuat. B* **1995**, *28*, 85.
[66] J. Rickert, W. Göpel, W. Beck, G. Jung, P. Heiduschka, *Biosens. Bioelectron.* **1996**, *11*, 757.
[67] H. Taira, K. Nakano, M. Maeda, M. Takagi, *Anal. Sci.* **1993**, *9*, 199.
[68] S. Ameur, C. Martelet, N. Jaffrezic-Renault, J. M. Chovelon, *Appl. Biochem. Biotechnol.* **2000**, *89*, 161.
[69] R. Blonder, E. Katz, Y. Cohen, N. Itzhak, A. Riklin, I. Willner, *Anal. Chem.* **1996**, *68*, 3151.
[70] V. M. Mirsky, M. Riepl, O. S. Wolfbeis, *Biosens. Bioelectron.* **1997**, *12*, 977.
[71] O. Ouerghi, A. Touhami, N. Jaffrezic-Renault, C. Martelet, H. Ben Ouada, S. Cosnier, *Bioelectrochemistry* **2002**, *56*, 131.
[72] C.-D. Feng, Y.-D. Ming, P. J. Hesketh, S. M. Gendel, J. R. Stetter, *Sens. Actuat. B* **1996**, *35*, 431.
[73] S. Ameur, C. Martelet, N. Jaffrezic-Renault, J. M. Chovelon, C. Plossu, D. Babier, *Proc. Electrochem. Soc.* **1997**, *19*, 1019.
[74] M. Jie, C. Y. Ming, D. Jing, L. S. Cheng, L. Huaina, F. Jun, C. Y. Xiang, *Electrochem. Commun.* **1999**, *1*, 425.
[75] F. Patolsky, B. Filanovsky, E. Katz, I. Willner, *J. Phys. Chem. B* **1998**, *102*, 10359.
[76] I. Willner, B. Willner, *Biotechnol. Prog.* **1999**, *15*, 991.
[77] A. Sargent, T. Loi, S. Gal, O. A. Sadik, *J. Electroanal. Chem.* **1999**, *470*, 144.
[78] G. Lillie, P. Payne, P. Vadgama, *Sens. Actuat. B* **2001**, *78*, 249.
[79] G. Farace, G. Lillie, T. Hianik, P. Payne, P. Vadgama, *Bioelectrochemistry* **2002**, *55*, 1.
[80] O. Ouerghi, A. Senillou, N. Jaffrezic, C. Martelet, H. Ben Ouada, S. Cosnier, *J. Electroanal. Chem.* **2001**, *501*, 62.
[81] H. Maupas, A. P. Soldatkin, C. Martelet, N. Jaffrezic, B. Mandrand, *J. Electroanal. Chem.* **1997**, *421*, 165.
[82] I. Willner, R. Blonder, A. Dagan, *J. Am. Chem. Soc.* **1994**, *116*, 9365.
[83] R. Blonder, S. Levi, G. Tao, I. Ben-Dov, I. Willner, *J. Am. Chem. Soc.* **1997**, *119*, 10467.
[84] L. Alfonta, A. Bardea, O. Khersonsky, E. Katz, I. Willner, *Biosens. Bioelectron.* **2001**, *16*, 675.
[85] E. Katz, L. Alfonta, I. Willner, *Sens. Actuat. B* **2001**, *76*, 134.
[86] L. Alfonta, I. Willner, D. J. Throckmorton, A. K. Singh, *Anal. Chem.* **2001**, *73*, 5287.
[87] H. C. Yoon, H. Yang, Y. T. Kim, *Analyst* **2002**, *127*, 1082.
[88] C. M. Ruan, L. J. Yang, Y. B. Li, *Anal. Chem.* **2002**, *74*, 4814.
[89] R. Pei, Z. Cheng, E. Wang, X. Yang, *Biosen. Bioelectron.* **2001**, *16*, 355.
[90] L. Alfonta, A. K. Singh, I. Willner, *Anal. Chem.* **2001**, *73*, 91.
[91] C. J. McNeil, D. Athey, M. Ball, W. O. Ho, S. Krause, R. D. Armstrong, J. D. Wright, K. Rawson, *Anal. Chem.* **1995**, *67*, 3928.
[92] W. O. Ho, S. Krause, C. J. McNeil, J. A. Pritchard, R. D. Armstrong, D. Athey, K. Rawson, *Anal. Chem.* **1999**, *71*, 1940.
[93] J. Wang, *Nucleic Acid Res.* **2000**, *28*, 3011.
[94] J. Wang, E. Palecek, P. E. Nielsen, G. Rivas, X. Cai, H. Shiraishi, N. Dontha, D. Luo, P. A. M. Farias, *J. Am. Chem. Soc.* **1996**, *118*, 7667.
[95] W. C.I. Homs, *Anal. Lett.* **2002**, *35*, 1875.
[96] S. R. Mikkelsen, *Electroanalysis* **1996**, *8*, 15.
[97] E. K. Wilson, *Chem. Eng. News* **1998**, *76*, 47.
[98] K. M. Millan, S. R. Mikkelsen, *Anal. Chem.* **1993**, *65*, 2317.
[99] M. S. Yang, M. E. McGovern, M. Thompson, *Anal. Chim. Acta* **1997**, *364*, 259.
[100] A. M. Oliveira-Brett, C. M. A. Brett, L. A. Silva, *Bioelectrochemistry* **2002**, *56*, 33.
[101] A. M. Oliveira-Brett, L. A. da Silva, C. M. A. Brett, *Langmuir* **2002**, *18*, 2326.
[102] E. Lust, A. Jänes, K. Lust, *J. Electroanal. Chem.* **1998**, *449*, 153.
[103] C. M. A. Brett, A. M. O. Brett, S. H. P. Serrano, *Electrochim. Acta* **1999**, *44*, 4233.
[104] Y.-D. Zhao, D.-W. Pang, S. Hu, Z.-L. Wang, J.-K. Cheng, Y.-P. Qi, H.-P. Dai, B.-W. Mao, Z.-Q. Tian, J. Luo, Z.-H. Lin, *Anal. Chim. Acta* **1999**, *388*, 93.
[105] B. Saoudi, C. Despas, M. M. Chehimi, N. Jammul, M. Delamar, J. Bessière, A. Walcarius, *Sens. Actuat. B* **2000**, *62*, 35.
[106] F. Lisdat, B. Ge, B. Krause, A. Ehrlich, H. Bienert, F. W. Scheller, *Electroanalysis* **2001**, *13*, 1225.
[107] L. Strašák, J. Dvoøak, S. Hasoò, V. Vetterl, *Bioelectrochemistry* **2002**, *56*, 37.
[108] F. Patolsky, A. Lichtenstein, I. Willner, *J. Am. Chem. Soc.* **2001**, *123*, 5194.
[109] G. Wang, J.-J. Xu, H.-Y. Chen, *Electrochem. Commun.* **2002**, *4*, 506.
[110] L. Luo, J. Liu, Z. Wang, X. Yang, S. Dong, E. Wang, *Biophys. Chem.* **2001**, *94*, 11.
[111] R. Pei, X. Cui, X. Yang, E. Wang, *Biomacromolecules* **2001**, *2*, 463.
[112] S. Hason, J. Dvorák, F. Jelen, V. Vetterl, *Critical Rev. Anal. Chem.* **2002**, *32*, 167.
[113] F. Yan, O. A. Sadik, *Anal. Chem.* **2001**, *73*, 5272.
[114] F. Yan, O. A. Sadik, *J. Am. Chem. Soc.* **2001**, *123*, 11335.
[115] S. Hasoò, J. Dvoøak, F. Jelen, V. Vetterl, *Talanta* **2002**, *56*, 905.
[116] A. Bardea, F. Patolsky, A. Dagan, I. Willner, *Chem. Commun.* **1999**, 21.
[117] F. Patolsky, A. Lichtenstein, I. Willner, *Angew. Chem. Int. Ed.* **2000**, *39*, 940.
[118] F. Patolsky, E. Katz, A. Bardea, I. Willner, *Langmuir* **1999**, *15*, 3703.
[119] F. Patolsky, E. Katz, I. Willner, *Angew. Chem. Int. Ed.* **2002**, *41*, 3398.
[120] F. Patolsky, A, Lichtenstein, I. Willner, *Nature Biotechnol.* **2001**, *19*, 253.
[121] F. Patolsky, A. Lichtenstein, M. Kotler, I. Willner, *Angew. Chem. Int. Ed.* **2001**, *40*, 2261.
[122] L. Alfonta, I. Willner, *Chem. Comm.* **2001**, 1492.
[123] J. J. Gooding, *Electroanalysis* **2002**, *14*, 1149.
[124] M. Y. Vagin, A. A. Karyakin, T. Hianik, *Bioelectrochemistry* **2002**, *56*, 91.
[125] D. J. Caruana, A. Heller, *J. Am. Chem. Soc.* **1999**, *121*, 769.

[126] J. M. Chovelon, N. Jaffrezic-Renault, Y. Gross, J. J. Fombon, D. Pedone, *Sens. Actuat. B* **1991**, *3*, 43.
[127] L. Bousse, P. Bergveld, *J. Electroanal. Chem.* **1983**, *152*, 25.
[128] B. Prasad, R. Lal, *Meas. Sci. Technol.* **1999**, *10*, 1097.
[129] H. Maupas, C. Saby, C. Martelet, N. Jaffrezic-Renault, A. P. Soldatkin, M.-H. Charles, T. Delair, B. Mandrand, *J. Electroanal. Chem.* **1996**, *406*, 53.
[130] C. Schyberg, C. Plossu, D. Barbier, N. Jaffrezic-Renault, C. Martelet, H. Maupas, E. Souteyrand, M.-H. Charles, T. Delair, B. Mandrand, *Sens. Actuat. B* **1995**, *26–27*, 457.
[131] N. Jaffrezic-Renault, C. Martelet, *Synth. Metals* **1997**, *90*, 205.
[132] H. Berney, J. Alderman, W. Lane, J. K. Collins, *Sens. Actuat. B* **1997**, *44*, 578.
[133] E. Souteyrand, J. R. Martin, C. Martelet, *Sens. Actuat. B* **1994**, *20*, 63.
[134] P. Bergveld, *Biosens. Bioelectron.* **1991**, *6*, 55.
[135] C. Saby, N. Jaffrezic-Renault, C. Martelet, B. Colin, M.-H. Charles, T. Delair, B. Mandrand, *Sens. Actuat. B* **1993**, *16*, 458.
[136] P. Bataillard, P. Clechet, N. Jafferzic-Renault, X. G. Kong, C. Martelet, *Sens. Actuat.* **1987**, *12*, 245.
[137] J. L. Diot, J. Joseph, J. R. Martin, P. Clechet, *J. Electroanal. Chem.* **1985**, *193*, 75.
[138] F. Gardies, C. Martelet, B. Colin, B. Mandrand, *Sens. Actuat.* **1989**, *17*, 461.
[139] P. Bataillard, F. Gardies, N. Jafferzic-Renault, C. Martelet, B. Colin, B. Mandrand, *Anal. Chem.* **1988**, *60*, 2374.
[140] V. Billard, C. Martelet, P. Binder, J. Therasse, *Anal. Chim. Acta* **1991**, *249*, 367.
[141] A. Gebbert, M. Alvarez-Icaza, W. Stoecklein, R. D. Schmid, *Anal. Chem.* **1992**, *64*, 997.
[142] A. Sibai, D. Barbier, K. Elamri, N. Jaffrezic-Renault, E. Souteyrand, *Sens. Actuat. B* **1996**, *31*, 125.
[143] M. J. Schöning, A. Poghossian, *Analyst* **2002**, *127*, 1137.
[144] P. Bergveld, *Biosens. Bioelectron.* **1991**, *6*, 55.
[145] M. M. G. Antonisse, B. H. M. Snellink-Ruël, R. J. W. Lugtenberg, J. F. J. Engbersen, A. van den Berg, D. N. Reinhoudt, *Anal. Chem.* **2000**, *72*, 343.
[146] A. Friebe, F. Lisdat, W. Moritz, *Sens. Mater.* **1993**, *5*, 65.
[147] R. D. Armstrong, G. Horvai, *Electrochim. Acta* **1990**, *35*, 1.
[148] P. Bergveld, A. van den Berg, P. D. van der Waal, M. Skowronska-Ptasinska, E. J. R. Sudhölter, D. N. Reinhoudt, *Sens. Actuat. B* **1989**, *18*, 309.
[149] A. Demoz, E. M. J. Verporte, D. J. Harrison, *J. Electroanal. Chem.* **1995**, *389*, 71.
[150] A. B. Kharitonov, J. Wasserman, E. Katz, I. Willner, *J. Phys. Chem. B* **2001**, *105*, 4205.
[151] M. Zayats, O. A. Raitman, V. I. Chegel, A. B. Kharitonov, I. Willner, *Anal. Chem.* **2002**, *74*, 4763.
[152] A. B. Kharitonov, M. Zayats, A. Lichtenstein, E. Katz, I. Willner, *Sens. Actuat B* **2000**, *70*, 222.
[153] C. A. Marquette, I. Lawrence, C. Polychronakos, M. F. Lawrence, *Talanta* **2002**, *56*, 763.
[154] J. P. Cloarec, N. Deligianis, J. R. Martin, I. Lawrence, E. Souteyrand, C. Polychronakos, M. F. Lawrence, *Biosens. Bioelectron.* **2002**, *17*, 405.
[155] J. P. Cloarec, J. R. Martin, C. Polychronakos, I. Lawrence, M. F. Lawrence, E. Souteyrand, *Sens. Actuat. B* **1999**, *58*, 394.
[156] E. Souteyrand, C. Chen, J. P. Cloarec, X. Nesme, P. Simonet, I. Navarro, J. P. Martin, *Appl. Biochem. Biotechnol.* **2000**, *89*, 195.
[157] E. Souteyrand, J. P. Cloarec, J. R. Martin, C. Wilson, I. Lawrence, S. Mikkelsen, M. F. Lawrence, *J. Phys. Chem. B* **1997**, *101*, 2980.
[158] I. Willner, E. Katz, A. Riklin, R. Kasher, *J. Am. Chem. Soc.* **1992**, *114*, 10965.
[159] I. Willner, V. Heleg-Shabtai, R. Blonder, E. Katz, G. Tao, A. F. Bückmann, A. Heller, *J. Am. Chem. Soc.* **1996**, *18*, 10321.
[160] M. Zayats, E. Katz, I. Willner, *J. Am. Chem. Soc.* **2002**, *124*, 14724.
[161] V. Pardo-Yissar, E. Katz, I. Willner, A. B. Kotlyar, C. Sanders, H. Lill, *Faraday Discuss.* **2000**, *116*, 119.
[162] I. Willner, A. Riklin, B. Shoham, D. Rivenzon, E. Katz, *Adv. Mater.* **1993**, *5*, 912.
[163] B. Liedberg, C. Nylander, I. Lundsröm, *Biosens. Bioelectron.* **1995**, *10*, R1.
[164] H. Elwing, *Biomaterials* **1998**, *19*, 397.
[165] L. Alfonta, E. Katz, I. Willner, *Anal. Chem.* **2000**, *72*, 927.
[166] F. Patolsky, M. Zayats, E. Katz, I. Willner, *Anal. Chem.* **1999**, *71*, 3171.
[167] E. J. Calvo, R. Etchenique, C. Danilowicz, L. Diaz, *Anal. Chem.* **1996**, *68*, 4186.
[168] A. G. E. Saum, R. H. Cumming, F. J. Rowell, *Biosens. Bioelectron.* **2000**, *15*, 305.
[169] A. G. E. Saum, R. H. Cumming, F. J. Rowell, *Biosens. Bioelectron.* **1998**, *13*, 511.
[170] J. G. Gu, S. P. Cheng, J. H. Liu, J. D. Gu, *J. Polym. Environ.* **2000**, *8*, 167.
[171] C. Bonazzola, E. J. Calvo, *J. Electroanal. Chem.* **1998**, *449*, 111.
[172] E. Katz, D. D. Schlereth, H.-L. Schmidt, *J. Electroanal. Chem.* **1994**, *367*, 59.
[173] A. Otero, M.-L. Garcia-López, B. Moreno, *Meat. Sci.* **1998**, *49*, S179.
[174] D. Ivnitski, I. Abdel-Hamid, P. Atanasov, E. Wilkins, S. Stricker, *Electroanalysis* **2000**, *12*, 317.
[175] J. E. Moore, R. H. Madden, *J. Food Protection* **2002**, *65*, 1660.
[176] A. L. Lafargue, L. B. Cabrales, R. M. Larramendi, *Bioelectromagnetics* **2002**, *23*, 450.
[177] A. Abdelghani, C. Abdelghani-Jacquin, H. Hillebrandt, E. Sackmann, *Mater. Sci. Eng. C* **2002**, *22*, 67.
[178] T. Nacke, M. Anhalt, D. Frense, D. Beckmann, *Technisches Messen* **2002**, *69*, 12.
[179] K. G. Ong, J. Wang, R. S. Singh, L. G. Bachas, C. A. Grimes, *Biosens. Bioelectron.* **2001**, *16*, 305.
[180] J. H. T. Luong, M. Habibi-Rezaei, J. Meghrous, C. Xiao, K. B. Male, A. Kamen, *Anal. Chem.* **2001**, *73*, 1844.
[181] A. Reininger-Mack, H. Thielecke, A. A. Robitzki, *Trends Biotechnol.* **2002**, *20*, 56.
[182] T. Ichiki, S. Shinbashi, T. Ujiie, Y. Horiike, *J. Photopolymer Sci. Technol.* **2002**, *15*, 487.
[183] E. Prokhorov, F. Llamas, E. Morales-Sanchez, J. Gonzalez-Hernandez, A. Prokhorov, *Med. Biol. Eng. Comp.* **2002**, *40*, 323.
[184] J. Jossinet, E. Marry, A. Matias, *Phys. Med. Biol.* **2002**, *47*, 2189.
[185] N. Sallacan, M. Zayats, T. Bourenko, A. B. Kharitonov, I. Willner, *Anal. Chem.* **2002**, *74*, 702.
[186] P. Schroth, H. Lüth, H. E. Hummel, S. Schütz, M. J. Schöning, *Electrohim. Acta* **2001**, *47*, 293.